

ABSTRACT

WAN, ZHAO. Design of a Stator Permanent Magnet Transverse Flux Machine for Direct-drive Application. (Under the direction of Dr. Iqbal Husain).

Transverse Flux Machines have attracted strong research interest in the past 20 years particularly due to the availability of soft magnetic cores making three dimensional flux path easier to implement. TFM's high torque density makes it a suitable candidate for low-speed, direct-drive applications. State of the art TFM designs often require the use of high energy density rare earth magnets, which is subject to issues of price fluctuation in rare earth metals, physical damage from chip and corrosion, eddy current loss, and demagnetization risk at high temperatures. Low cost ferrite magnet is a good alternative to use in TFMs. Nonetheless, ferrite magnet has very low energy density, thus is more prone to rotor-leakage-flux and low power factor issues, such that few TFM topology exists in the literature that can effectively use ferrite magnets for a high torque density design.

This dissertation explores novel designs of the TFM rotor that makes active use of all of the ferrite magnets and all of the air gap area that eliminates the flux leakage. On the stator side, this research tries to reduce armature inductance through magnetic circuit modeling method with the aim of reducing the core saturation and improving power factor. Based on those studies, this dissertation proposes a novel Stator-PM TFM topology that achieves high torque density without using rare earth magnets. Through extensive electromagnetic, thermal and structural design and analysis, the proposed TFM topology demonstrates superior performance compare to other benchmark TFM machines. The new design is prototyped and experimentally tested to prove its suitability as a direct-drive motor that offers high torque density, high efficiency, low cogging torque, low cost and easy construction.

© Copyright 2018 by Zhao Wan

All Rights Reserved

Design of a Stator Permanent Magnet Transverse Flux Machine for Direct-drive Application

by
Zhao Wan

A dissertation submitted to the Graduate Faculty of
North Carolina State University
in partial fulfillment of the
requirements for the degree of
Doctor of Philosophy

Electrical Engineering

Raleigh, North Carolina

2018

APPROVED BY:

Dr. Iqbal Husain
Committee Chair

Dr. Srdjan Lukic

Dr. Rajib Mikail

Dr. Gregory Buckner

BIOGRAPHY

Zhao Wan received his bachelor's degree in Electrical Engineering from Yanshan University, China in 2011. He received his M. Sc. and Ph.D. degrees, both in Electrical Engineering, from North Carolina State University, Raleigh, NC in 2014 and 2018, respectively.

During his graduate school years at NCSU, his research involved design of high torque density electric machines for vehicle traction application, and control of switch reluctance machines for torque ripple minimization. During his internship in ABB Corporate Research Center in Raleigh, NC in 2015, he worked on the modeling and experimental testing of induction machines. His research interest covers design of permanent magnet and induction machines.

ACKNOWLEDGMENTS

I would like to thank Dr. Iqbal Husain for his guidance over five years in my Ph.D. studies. Accepting me as a Ph.D. student to work on this research project is a life changing moment for me. For this, I am forever grateful.

TABLE OF CONTENTS

LIST OF TABLES	vii
LIST OF FIGURES	viii
CHAPTER 1 TRANSVERSE FLUX MACHINE FOR LOW COST DIRECT DRIVE.....	1
1.1 The Need for Low Cost Direct-drive	1
1.2 Basics of Transverse Flux Machine.....	2
1.3 Direct-Drive TFM as Electromagnetically Geared Motor.....	4
1.4 Features of TFM	5
1.5 Research Objectives.....	8
CHAPTER 2 TFM WITH DOUBLE-SIDED STATOR.....	11
2.1 Previous Research on Rotor Flux Leakage.....	11
2.2 Double Stator Transverse Flux Machine	13
2.2.1 Rotor Flux Leakage Prevention	14
2.2.2 Rotor Flux Concentrator Design.....	16
2.2.3 Stator Core Shape and Winding Area.....	17
2.3 DESIGN AND PERFORMANCE OF A TWO-PHASE MACHINE.....	18
2.3.1 Two-Phase 800-W Motor for Scooter In-Wheel Application.....	19
2.3.2 No-Load Back-EMF	20
2.3.3 Electromagnetic Torque and Cogging Torque.....	21
2.3.4 Torque Density.....	22
2.4 Core Saturation	22
2.5 Conclusion	24
CHAPTER 3 INDUCTANCE ANALYSIS OF TFM	26
3.1 Saturation and Low Power Factor: the Issues with TFM Inductance.....	26
3.1.1 Relationship between armature inductance, rotor flux linkage, and power factor	26
3.1.2 Negative effects of high inductance.....	27
3.1.3 Inductance study towards a solution.....	28
3.2 TFM'S Inductance is Fundamentally Different.....	28
3.3 Inductance Analytical Equations and Design Guidelines	29
3.3.1 Air gap inductance	30
3.3.2 Slot leakage inductance.....	31
3.3.3 End winding inductance.....	32
3.3.4 Fringing inductance	32

3.3.5 Total inductance and power factor.....	33
3.4 Verification by 3D FEA Simulation	33
3.4.1 Simulation Method.....	34
3.4.2 Simulation Results	36
3.5 Conclusion	37
CHAPTER 4 STATOR-PM TRANSVERSE FLUX MACHINE.....	39
4.1 Stator-PM TFM Topology	40
4.2 Design and Optimization with 3D FEA.....	41
4.2.1 Torque, Efficiency and Power Factor	42
4.2.2 Cogging Torque	44
4.2.3 PM Demagnetization of Stator-PM TFM	45
4.2.4 Constant Power Speed Range	48
4.2.5 Efficiency Map for Entire Operating Region.....	50
4.3 Benchmark Comparison.....	52
4.4 Conclusions.....	53
CHAPTER 5 MULTI-PHYSICS DESIGN AND PROTOTYPE CONSTRUCTION.....	54
5.1 Structural Analysis.....	54
5.2 Thermal Analysis	57
5.3 Prototype Machine Construction	60
5.3.1 Winding.....	62
5.3.2 Stator	64
5.3.3 Rotor	66
5.3.4 Housing	67
5.4 Discrepancies between Initial Design and Finished Prototype.....	68
5.5 Conclusions.....	72
CHAPTER 6 EXPERIMENTAL SETUP AND TEST RESULTS	73
6.1 Experimental Setup.....	73
6.2 No-load Tests	74
6.2.1 Back-EMF.....	74
6.2.2 Cogging torque.....	76
6.2.3 Friction and windage loss	80
6.3 Torque Profile with Direct Current Excitation	81
6.4 Inductance Measurement and Short Circuit Test.....	84
6.5 Heat Run	87

6.6 Result Discussion.....	90
CHAPTER 7 CONTRIBUTION SUMMARY AND FUTURE WORK	91
REFERENCES	92

LIST OF TABLES

Table 2.1	Scooter Motor Design Parameters and Performances	19
Table 2.2	Summary of Parameters	23
Table 3.1	Compare TFM and FSCW PMSM.....	29
Table 4.1	List of Single Phase Stator-PM TFM Design Parameters and Values	42
Table 4.2	Benchmark Comparison for Stator-PM TFM.....	52
Table 5.1	Material Mechanical Properties.....	56
Table 5.2	Material Thermal Conductivity Parameter.....	58
Table 6.1	Summary of Resistance and Inductance Measurements with LCR Meter	85

LIST OF FIGURES

Figure 1.1	(a) Radial flux machine (b) Transverse flux machine	3
Figure 1.2	(a) TFM flux at aligned position 1 (b) TFM flux at unaligned position (c) TFM flux at aligned position 2	3
Figure 2.1	(a) AFG structure (b) Flux focusing concept (c) Solid model of AFG	12
Figure 2.2	(a) Solid model of single phase DS-TFM (b) PM magnetization and flux path	14
Figure 2.3	Flux linkage with and without alternating stators	15
Figure 2.4	(a) Rotor magnetization (b) Flux linkage with and without Halbach.....	16
Figure 2.5	Stator shape and core area corrections	18
Figure 2.6	Two-phase design with shifting between stator plates	20
Figure 2.7	Open-circuit back-EMF.....	21
Figure 2.8	Output torque and cogging torque.....	22
Figure 2.9	(a) DS-TFM has high inductance compared to Stator-PM TFM (b) Saturation of DS-TFM compared to Stator-PM TFM.....	24
Figure 3.1	(a) Typical PMSM power factor (b) Typical TFM power factor	26
Figure 3.2	(a) Front and side view of basic TFM topology (b) Basic TFM topology modeled in 3D FEA.....	30
Figure 3.3	(a) Slot leakage flux (b) End winding flux and fringing flux (c) Air gap flux (d) Air gap flux.....	35
Figure 3.4	(a) Slot leakage inductance with respect to width of slot W (b) Air gap inductance with respect to pitch factor K_s (c) Air gap inductance with respect to magnet thickness y_{PM} (d) End winding and fringing inductance with respect to K_s	36
Figure 3.5	Total inductance with respect to K_s	37
Figure 4.1	Stator-PM TFM topology	41
Figure 4.2	Stator-PM TFM flux path.....	41
Figure 4.3	(a) Torque vs. current density (b) Power factor, efficiency vs. current density.....	43

Figure 4.4	(a) Rotor tooth pitching shown in electrical degrees (b) Cogging torque (c) Three-phase torque ripple.....	44
Figure 4.5	(a) Armature flux with q -axis current (b) Armature flux with d -axis current (c) Flux in PM region	46
Figure 4.6	(a) PM flux density after peak q -axis current (b) PM flux density after peak d -axis current (c) PM flux density after ten times peak q -axis current (d) PM flux density before current loading	47
Figure 4.7	(a) Open circuit flux linkage before and after demagnetization (b) Electromagnetic torque before and after demagnetization.....	47
Figure 4.8	(a) Infinite drive system constant power operation (b) Stator-PM TFM torque speed curve and constant power speed range.....	49
Figure 4.9	Stator-PM TFM efficiency map.....	51
Figure 5.1	(a) Structural simulation Von Mises stress (b) Structural simulation Von Mises stress	56
Figure 5.2	(a) Rounded fillet (b) Von Mises stress with fillet (c) Von Mises stress with fillet	57
Figure 5.3	TFM model for thermal simulation.....	58
Figure 5.4	(a) Perfect contact scenario (b) Worst contact scenario.....	59
Figure 5.5	(a) TENV with $5 \text{ W/m}^2\cdot\text{K}$ (b) TEFV with $20 \text{ W/m}^2\cdot\text{K}$	60
Figure 5.6	TFM prototype stator structure design.....	61
Figure 5.7	(a) Winding bobbin (b) Ring winding with thin wire (c) Rectangular wire (d) Winding within bobbin (e) Finished winding (f) Winding with insulation.....	63
Figure 5.8	(a) Somaloy Prototyping Material blank (b) Stator core (c) Ferrite magnet blocks (d) One pole pair assembly (e) Finished stator with aluminum fixture.....	65
Figure 5.9	(a) Rotor Parts (b) Finished Rotor	67
Figure 5.10	(a) Stator and Rotor Fitted Inside Frame (b) Finished TFM Prototype.....	68
Figure 5.11	Back-EMF rms value as a function of airgap length.....	71
Figure 5.12	Measured and datasheet permanent magnet property	71
Figure 6.1	Experimental setup	74

Figure 6.2	(a) Back-EMF rms value with respect to speed (b) Experimental back-EMF waveform at 600 rpm (c) Experimental back-EMF harmonic spectrum.....	75
Figure 6.3	(a) Experimental cogging torque at 6 rpm for one mechanical cycle (b) Experimental cogging torque at 6 rpm harmonic distribution (c) Comparing experimental and FEA cogging torque at 6 rpm	78
Figure 6.4	(a) FEA simulated single phase and three phase cogging torque (b) Single phase cogging torque harmonics (c) Three phase cogging torque harmonics.....	79
Figure 6.5	(a) No load torque at various speeds (b) No load loss at various speeds	81
Figure 6.6	FEA simulated torque profile with direct current excitation.....	82
Figure 6.7	(a) Simulated and experimental torque profile with 5A dc excitation (b) Experimentally measured torque profile with dc excitation (c) Simulated and experimental peak torque with respect to dc current.....	83
Figure 6.8	(a) Simulated and measured leakage and total inductances (b) Terminal resistance measurement using LCR meter (c) Total winding inductance measurement using LCR meter.....	85
Figure 6.9	Simulated and experimental short circuit current at various speeds	87
Figure 6.10	Heat run temperature measurements.....	88

CHAPTER 1 TRANSVERSE FLUX MACHINE FOR LOW COST DIRECT DRIVE

1.1 The Need for Low Cost Direct-drive

Electric vehicle traction motor and wind turbine generator are two main areas that have seen increasing demand on high performance electric motors. The motors for these two applications share common performance requirements, namely high torque/power density, high efficiency, high reliability and low maintenance.

Traction motors in mass-market cars usually use NdFeB magnets, advanced liquid cooling, and a shiftless gearing stage. Megawatt-level wind turbines are configured with either a regular Permanent Magnet Synchronous Generator (PMSG) or Doubly-Fed Induction Generator (DFIG) plus a multi-stage gearbox, or with a direct-drive PMSG that requires large quantity of rare earth magnets. The usage of rare earth magnets, advanced cooling, and complex gearing certainly enables superior performance from the motors, but also adds manufacturing and maintenance cost. The extra cost and complexity might make sense in these applications, where advanced cooling and routine maintenance can be accommodated.

However, in applications like in electric scooter traction, or small residential wind generator, where liquid cooling is not an option, and where professional gearbox maintenance is not expected during the entire service life of the product, a low-cost air-cooled direct-drive motor without using rare-earth magnets becomes an attractive alternative. The above application constraints dictate the motor needs to have extremely high torque density, even using ferrite magnets and low current density. Transverse Flux Machines (TFM), widely known for its high torque capability, is a potentially suitable candidate for such applications.

1.2 Basics of Transverse Flux Machine

The machine got the Transverse Flux name because its flux path is not confined to any single plain but is three-dimensional in nature. However, the three dimensional flux path is only a characteristic feature of TFM, but not the fundamental difference that sets TFM apart from radial flux or axial flux machines. TFM's distinguishing identity lies in its monopolar concentrated ring winding.

Figure 1.1(a) illustrates a typical radial machine topology that has uniform stator with winding slots, where phase windings are distributed into each slot that belongs to particular poles. Each slot coil is only linked with the stator pole it is assigned to. The direction of the slot coils are arranged in alternating pattern that creates north and south magnetic poles. In this case, the air gap polarity is modulated by the alternation of the winding direction.

Figure 1.1(b) shows one phase module of the TFM that is distinguished by its concentrated ring winding. Segmented stator cores, usually C-shaped, are aligned circumferentially following the shape of the winding. The monopolar phase winding sits in the common slot of the stator poles, such that all the winding conductors are magnetically linked with all the stator poles. In this case, the shape of the stator poles modulates the winding MMF to create north and south magnetic poles at either end of the C-cores.

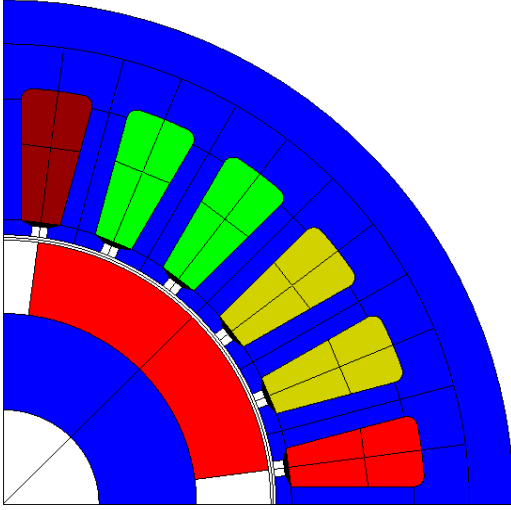


Figure 1.1. (a) Radial flux machine.

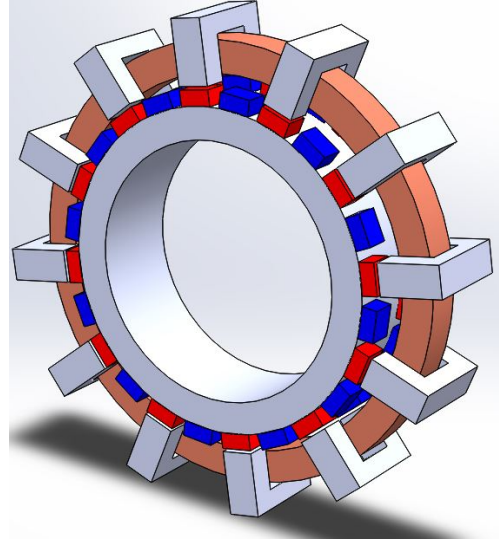


Figure 1.1. (b) Transverse flux machine.

Figure 1.2 shows flux path of the linearized two pole pairs of the basic TFM topology in detail. Each pole pair has a C-shaped stator core wrapped around the concentrated ring winding. Each rotor pole has a pair of surface mounted permanent magnets, with their polarities reversed between neighboring poles. In the first aligned rotor position, the direction of winding flux linkage is shown in Figure 1.2(a); in the unaligned position in Figure 1.2(b), the magnet flux closes through the tip of the stator poles without linking the stator winding; in the next aligned rotor position, the winding flux linkage reverses direction, as shown in Figure 1.2(c).

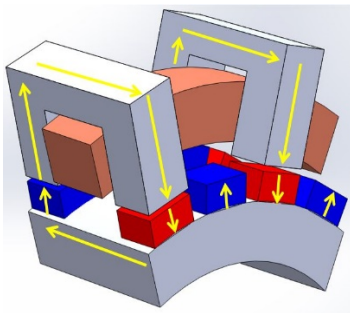


Figure 1.2. (a) TFM flux at aligned position 1.

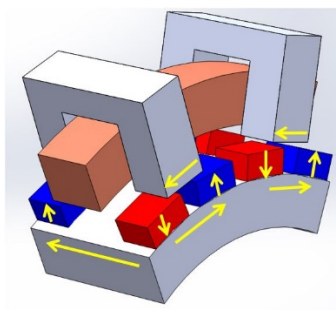


Figure 1.2. (b) TFM flux at unaligned position.

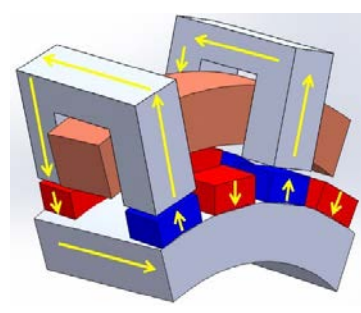


Figure 1.2. (c) TFM flux at aligned position 2.

Despite its unique structure, TFM's electrical circuit model and torque equation are essentially the same as those of regular PMSMs, herein listed below.

$$v_q = R_s i_q + \frac{d}{dt} \lambda_q + \omega_r \lambda_d \quad (1)$$

$$v_d = R_s i_d + \frac{d}{dt} \lambda_d - \omega_r \lambda_q \quad (2)$$

$$\lambda_q = L_q i_q \quad (3)$$

$$\lambda_d = L_d i_d + \lambda_f \quad (4)$$

$$Te = \frac{3P}{2} \lambda_f i_q = \frac{3}{2} \frac{\omega_e}{\omega_m} \lambda_f i_q \quad (5)$$

1.3 Direct-Drive TFM as Electromagnetically Geared Motor

Machine torque production follows Eq. (5), in which λ_f is winding flux linkage, representing magnetic loading; i_q is the conductor current, representing electrical loading; P is the pole number. In a multi-pole conventional machine with certain air gap diameter, the torque of the machine is limited by the competition of stator circumferential pole pitch between slots for conductors and teeth for iron. Use the torque equation Eq. (5) as an example, doubling the pole number P at the same time also halves the space for winding and flux linkage λ_f , resulting in no increase in torque.

In contrast, for TFM the physical space for magnetic flux and electrical current are decoupled. All the conductors in the ring winding links with all the stator poles, such that an increase in pole number does not affect the number of conductor turns per pole. Therefore, in ideal theoretical condition, which ignores leakage and saturation, TFM is able to increase its pole number P without sacrificing the total flux linkage λ_f . Consequently, at a certain input electrical power and frequency, the TFM's magnetic loading remains constant even with doubled pole number, giving the high pole machine doubled torque output at half the mechanical speed.

The author considers direct-drive TFM as electromagnetically geared motor in replace of mechanical gearing. By using a high pole number, TFM extends the ratio between high input electrical frequency and low output mechanical speed, in exchange for proportionally high output torque. The TFM trades off rotational speed to gain augmentation in output torque, just as a mechanical gear uses mechanical advantage to trade off movement to obtain force amplification.

1.4 Features of TFM

Previous researches have demonstrated TFM is suitable for low-speed high-torque direct-drive applications, particularly because of advantages in high torque density and high efficiency. The same researches also revealed the challenges facing TFM. By reviewing previous literature and current application, this section brings together both advantages and drawbacks of TFM.

1.4.1 TFM has high torque density

Research on TFM first gained momentum in the 1990s thanks to its high torque density. Several research projects in University of Southampton [1] and University of Newcastle [2] worked on different topologies of TFM, all of which are capable of very high torque per unit volume of active components. Study in [3] evaluated Transverse Flux topology against radial and axial flux topologies for ‘in-wheel’ motor application, and concluded that transverse flux motors have higher torque density and efficiency, but suffers from poor power factor.

1.4.2 TFM has short winding and high efficiency

Electric Torque Machines Inc. [4] patented and commercialized an industrial direct-drive TFM, which delivers 3 times more torque than a conventional motor while uses only about half amount of copper. The short winding length only has 0.017 Ohm of resistance, which boosts machine efficiency by reducing stator copper loss.

1.4.3 TFM is easy to cool

A few researches noted the thermal aspects of TFM [5]. Conventional machine cooling wisdom has concluded that the end winding is most prone to overheating [6], because the end part of the machine is exposed to enclosed air, without direct contact with metal material as heat path. TFM, on the other hand, has little to none exposed end winding. TFM's concentrated stator winding, where most of loss is located for a direct-drive motor, is usually in close contact with stator iron material, through which heat from copper loss can dissipate.

1.4.4 TFM has excellent reliability

Modular components are easy to manufacture, assemble, repair and replace, and highly fault tolerant. Multi-phase TFM is simple axial stacking of any number of identical single-phase modules. The physically and magnetically independent phases are beneficial for fault tolerance. The demonstrator program by Rolls-Royce plc and Royal Navy [7] built a 20MW TFM for the direct-drive propulsion of ships, and particularly highlighted TFM's mechanical integrity and fault tolerance capability.

1.4.5 TFM has potential for low cost production

The authors in [9] built and tested a TFM prototype using Soft Magnetic Composite (SMC) material, and demonstrated that TFM with SMC is superior in specific torque and power to induction motor, at the same time offers potential in reducing manufacturing cost. The Combined-Phase TFM design in [10] only uses four stator SMC components, each of which comes from a single compaction, thus leads to cost reduction by employing fewer assembly stages. The experimental study in [10] also credits TFM's modular pole and preformed winding for potential reduction in tooling and labor cost.

1.4.6 TFM has poor magnet utilization

Earlier version of TFM [11] suffers from very inefficient utilization of rotor magnets. The authors in [12] and [13] studied the extent of rotor flux leakage in such machines, and observed that the majority of rotor flux failed to contribute to stator winding flux linkage. Such a failure not only negatively affects torque and efficiency, but also demands the use of larger volume of permanent magnets.

1.4.7 TFM suffers from low power factor

TFM is notorious for its extremely low power factor [14], one reason of which is the above mentioned poor magnet utilization. Aside from that, [12] identified another more important reason as TFM having a very high inductance and high electric loading. As a result, the magnitude of armature reaction is usually several times that of the back-emf, driving low the TFM's power factor. Low power factor requires inverter with much higher power rating than the TFM, adding cost to the motor drive system.

1.4.8 TFM is difficult to use lamination

Conventional machines use laminated electrical steel for stator and rotor cores to reduce eddy current loss. The cores of TFM is difficult to build using lamination, because TFM requires three-dimensional flux path, while the lamination can only conduct flux in a two-dimensional plane. The authors in [15] devised a plan to build TFM using segmented lamination, which consists of an assembly of lamination segments that are aligned in either radial/circumferential or radial/axial directions. However, such a construction scheme reduces mechanical reliability and inevitably puts more difficulty on manufacturing.

1.5 Research Objectives

The main objective of this research is to solve or improve the identified drawbacks in the current TFM topologies, and to make TFM an attractive and feasible solution for direct-drive applications. Other objectives include:

- Design a ferrite magnet based, air-cooled, modular structured, and easily manufactured TFM for low cost direct drive traction application.
- The designed TFM should have flux concentration feature, and effectively utilize the all the magnets and entire air gap area, with minimal rotor flux leakage.
- Based on fundamental understanding and physical modeling, propose TFM design guidelines that tackle low power factor issue for all TFM topologies.
- Explore other performance aspects that are previously ignored in TFM research, such as thermal study on TFM, demagnetization study on stator ferrite magnets, cogging torque reduction, field weakening operation and CPSR.

1.6 Outline of this Report and Subsequent Research Plan

Chapter 2: TFM with Double-Sided Stator

This chapter first reviews successes and shortcomings in recent research attempts in tackling TFM's rotor flux leakage issue. Then a new Double-Sided TFM is proposed that makes full use of rotor ferrite magnets and the entire air gap, and effectively eliminates rotor flux leakage. Based upon optimization of the DS-TFM topology, the author designs a two-phase traction motor for electric scooter application. The designed motor exhibits satisfactory torque and efficiency, but suffers from low power factor and severe core saturation that prevented it from achieving its expected potential in torque density.

Chapter 3: Inductance Analysis of TFM

Having recognized high inductance as the key shortcoming that plagues TFM's performance, this chapter aims to conduct comprehensive study on TFM's inductance. First, comparison of TFM and conventional PMSM reveals the underlying reason for TFM's high inductance and low power factor. Then, the proposed magnetic circuit model separates total inductance into individual components based on distinct flux paths, and linked each inductance component to key geometric parameters. The qualitative and quantitative study helps to gain deeper understanding of the TFM's inductance and power factor from a fundamental and physical perspective, and draws the conclusion that even though TFM has an unavoidably high inductance, there is room for improvement through geometric design changes. Design guidelines are then proposed and verified by 3D FEA simulation as a solution to reduce TFM's inductance and minimize the inherent saturation problem.

Chapter 4: Design of Stator PM TFM

Building upon the knowledge gained through study in the first three chapters, this chapter aims to design the best possible TFM for direct-drive traction application, with the constraints of using ferrite magnets, air-cooling, and maintaining modularity in construction. The resulting Stator-Magnet TFM topology excels in various performance aspects, including resistance to PM demagnetization, low cogging torque, extended constant power speed range, and high efficiency in the majority of operating region. In comparison with representative benchmark machines, the designed TFM exhibits balanced performance in terms of torque density, efficiency and power factor.

Chapter 5: Multi-physics Design and Prototype

This chapter describes the multi-physics design, calculation and simulation of the machine, as well as the process of successfully building a one horsepower stator-PM TFM prototype, which will be used to in experimental tests to verify the electromagnetic design and performance. The modular structure, concentrated winding, and inner solid rotor configuration all contribute to easier automation and lower cost for mass production. Steady state thermal analysis under various boundary conditions predicts the thermal performance of the prototype motor, and serves as a guideline for designing the thermal path.

Chapter 6: Experimental Evaluation

This chapter details the experimental setup for testing the TFM prototype, and the various tests performed to evaluate the electromagnetic and thermal performance. Test results provide both instantaneous waveforms and averaged steady state measurements. The experimental results are then compared with those from FEA simulation to offer more insight, and to provide valuable feedback information in retuning the simulation model.

CHAPTER 2 TFM WITH DOUBLE-SIDED STATOR

The rotor flux leakage issue identified in Chapter 1 is one major drawback that stymied the early versions of TFM topologies from achieving their expected potential in torque density. This chapter first looks at several previous researches that have tried to tackle this issue and achieved partial success. Then, building upon the knowledge gained from these researches, a new double-sided stator TFM topology is proposed that completely solves the rotor flux leakage problem. Lastly, detailed study on the new topology reveals high inductance, core saturation, and construction challenges that demand further improvements.

2.1 Previous Research on Rotor Flux Leakage

The “TFM with bridge” topology introduced in [16], as well as the “magnetic shunt” concept proposed in [17] successfully prevented the inactive magnets from producing damaging negative flux linkage by providing a short circuit flux path. However, only half of the rotor magnets contribute to flux linkage with stator winding, with the other half staying idle.

By deploying double-winding per phase, the topology described in [18][19] makes active use of all the rotor magnets at every aligned position. The rotor is only compatible with surface-mounted rare-earth NdFeB magnets. However, replacing NdFeB with low energy ferrite magnets, which is a main objective of this thesis, requires rotor arrangements that enable flux focusing.

The Axial Flux Generator (AFG) in [10] serves as a major inspiration for the design proposed in this chapter. Shown in Figure 2.1(a), the AFG has double stator in each phase. The rotor of AFG sits between the stator plates, and in each pole has one piece of magnet sandwiched between two pieces of iron core. The rotor utilizes flux-focusing technique that concentrates the magnets’ flux into the air gap, thus enabling high flux density in the air gap with low energy ferrite magnets. Figure 2.1(b) explains the flux concentration concept by showing 2D FEA simulated flux path and

flux density. Figure 2.1(c) illustrates the three dimensional model of the single phase AFG, in which C-shaped stator cores only surround every other pole of the stator coil, therefore leaving half the coil as end winding, and half the air gap area unutilized.

The new TFM topology to be introduced in this chapter uses the AFG as the starting point, making design improvements that eliminate the end winding and make full use of the available air gap area, effectively doubling the open circuit flux linkage.

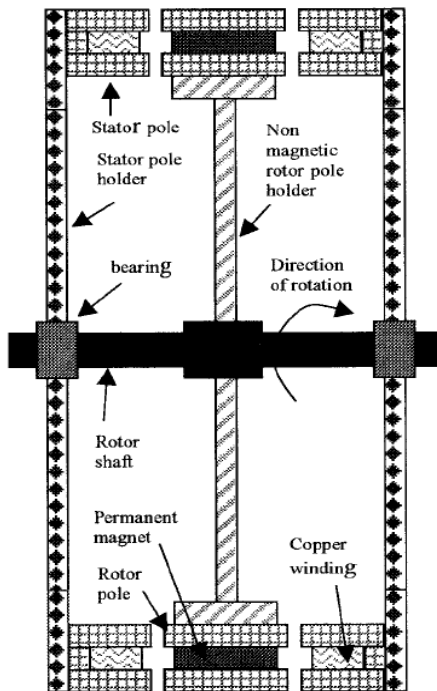


Figure 2.1. (a) AFG structure.

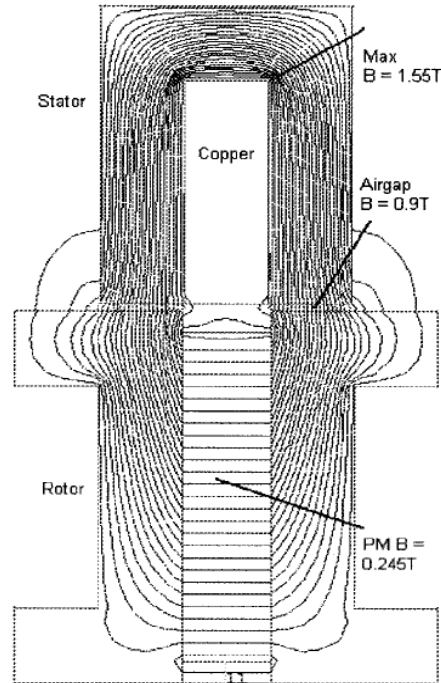


Figure 2.1. (b) Flux focusing concept.

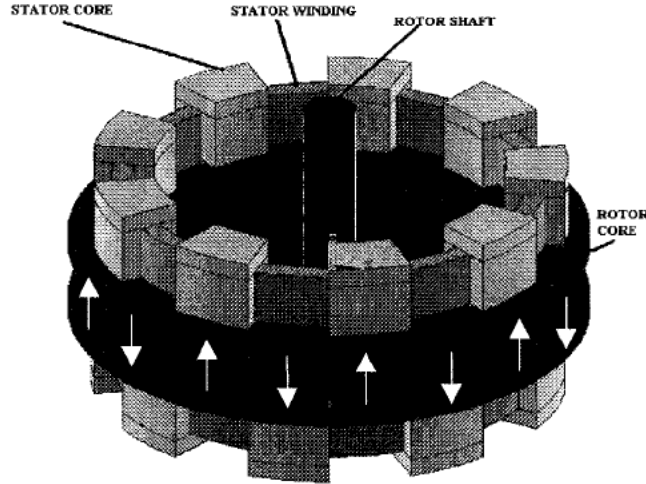


Figure 2.1. (c) Solid model of AFG.

2.2 Double Stator Transverse Flux Machine

An illustration of the proposed concept machine is given in Figure 2.2. Figure 2.2(a) shows the solid model for one module or phase of the machine. The rotor is in the middle, and the stator cores and windings are located on both sides of the rotor. Cross section view in Figure 2.2(b) illustrates the permanent magnet (PM) magnetization and flux path of the proposed TFM. The sandwiched magnets between the rotor cores allow redirecting the flux direction produced by the permanent magnets. The magnet directions are alternately arranged so that the north poles of the two magnets point either toward or away from each other.

The clockwise direction of the flux in the stator core (top left in Figure 2.2(b) encircling coil winding W1) indicates that the current flows in the top coils in the same direction. The magnetic polarity of the magnets is pointing toward the middle rotor core. The flux leaving the middle rotor core enters the stator core, flows in a clockwise direction, exits at the top of the stator core, and enters the top of the rotor pole. The flux direction in the stator core (top right in Figure 2.2(b) encircling coil winding W2) is also clockwise. The flux leaving the middle rotor core enters the stator core, flows in a clockwise direction, exits at the bottom of the stator core, and enters the bottom of the rotor pole.

One pole that is behind this rotor pole is not visible, but it is shown on the right side of Figure 2.2(b). The magnetic polarity of this rotor pole is the opposite of the previous rotor pole. The direction points away from the middle rotor core. The flux leaving the top rotor core enters the stator core at the top, flows in a clockwise direction, and exits at the bottom of the stator core into the middle core. The bottom cross-sectional diagram in Figure 2.2(b) shows that the counterclockwise direction is consistent with the direction of the current in the winding, as indicated by the top cross-sectional diagram.

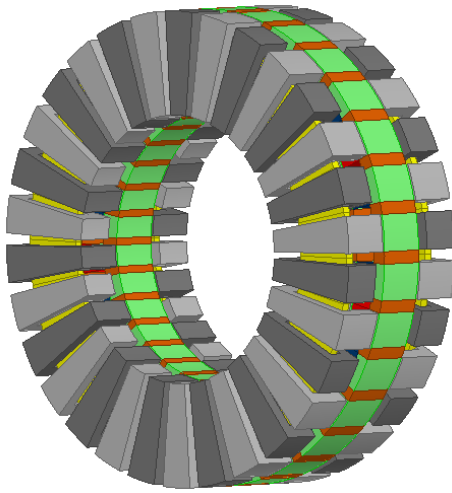


Figure 2.2. (a) Solid model of single phase DS-TFM.

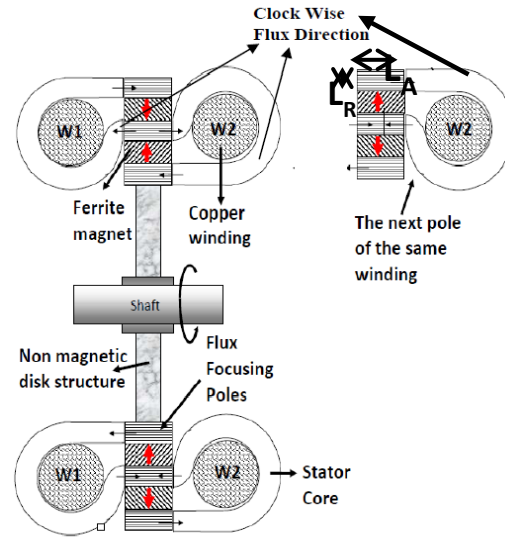


Figure 2.2. (b) PM magnetization and flux path.

2.2.1 Rotor Flux Leakage Prevention

TFMs suffer from poor rotor magnet flux utilization primarily for two reasons. One, according to [1][17], is that when one magnet is in the aligned position to establish flux linkage, the neighboring magnets with opposite polarity produce fringing flux that subtracts from the total back-EMF-inducing flux. Another reason is because of the direct leakage flux in the circumferential direction between neighboring heteropolar magnets [20].

Magnetic shunts were introduced in [17] to counter the negative effect of fringing flux; however, the shunts only passively direct the fringing flux away from the main flux path. In the proposed machine structure, the alternating stator core design makes active use of all the rotor magnets to build flux linkage in the coil, such that what would have been fringing flux are equally utilized to induce back-EMF. FEA simulation results in Figure 2.3 show that when two sets of alternating stator cores are used, the coil flux linkage more than doubles compared to when only one set of cores is used.

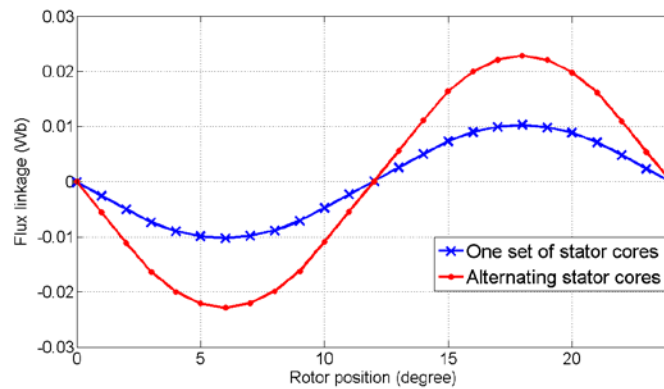


Figure 2.3. Flux linkage with and without alternating stators.

One common way to reduce inter-polar flux leakage is to increase the physical separation and thus also increase the magnetic reluctance between rotor magnets, but this also sacrifices effective pole face area. In the proposed design innovation, extra magnets are put into the separation between the rotor poles, and they are magnetized in the direction opposing inter-polar leakage, as shown in Figure 2.4(a). Such a magnet arrangement when combined with rotor cores creates a flux pattern similar to that of a Halbach array [21]. Thus, instead of passively relying on the air reluctance to suppress flux leakage, the spaces are actively utilized to contribute to flux linkage. As shown in Figure 2.4(b), by using extra “Halbach magnets,” flux linkage is increased by 90% compared to the case without them.

To determine the optimal thickness of the Halbach magnets, a rotor separation factor K_r is defined as

$$K_r = \frac{\theta_R}{\theta_P} \quad (1)$$

in which, as shown in Figure 2.4(a), θ_R is the rotor arc span, and θ_P is the pole pitch. The thickness of the Halbach magnets is proportional to $1 - K_r$. Based on 3D FEA simulation, to maximize winding flux linkage the optimum value for K_r is 0.65, which provides a large enough pole face area while at the same time maintains a reasonable thickness for the Halbach magnets.

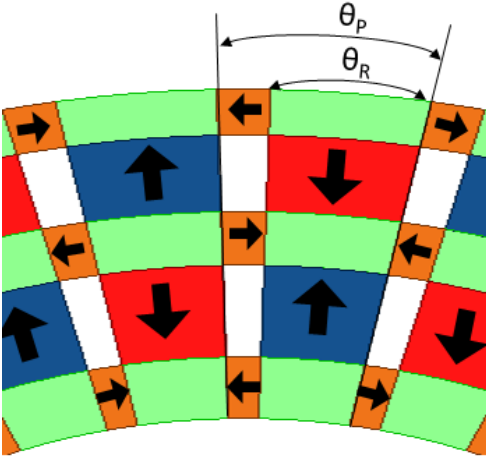


Figure 2.4. (a) Rotor magnetization.

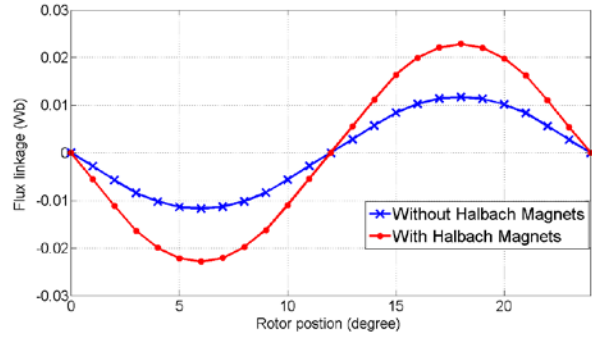


Figure 2.4. (b) Flux linkage with and without Halbach.

2.2.2 Rotor Flux Concentrator Design

Magnetic flux in the rotor is guided by the metal parts, which are referred to as flux concentrators. Such naming is reasonable because these segments are designed in a manner that increases the flux density in the air gap compared to that along the magnet cross sections. Because ferrite magnets exhibit lower remnant flux density, careful design of these rotor flux concentrators results in a higher air-gap flux density, comparable to that achieved by stronger rare-earth material magnets. The concept can be better visualized from the cross-sectional view shown in Figure 2.2(b). The magnetic flux path in the radial plane is proportional to the axial length of the magnet

labeled L_A . The rotor pole area exposed to the air gap is proportional to the radial length of the corresponding flux concentrator, labeled L_R , for the outermost rotor segment shown in Figure 2.2(c). Thus, the concentration factor can then be defined as

$$\text{Concentration Factor } K_f = \frac{L_A}{L_R} \quad (2)$$

The operating flux density inside the magnets can be roughly estimated considering the infinitely permeable stator and rotor metal area and is given by

$$B_m = \frac{M_L}{2 \times \text{Airgap} \times K_f + M_L} \quad (3)$$

Here, M_L = Magnet radial length

The air-gap flux density is simply magnified by the concentration factor K_f and can be given as

$$B_{AG} = B_m \times K_f \quad (4)$$

Because the operating point of the magnet reduces with a higher concentration factor, there exists an optimum point that maximizes flux linkage. Considering a nonlinear BH curve for the core material, the optimum concentration factor depends on the magnetic saturation of metal, remnant flux density of the magnets, air gap, and number of pole pairs in the design.

In another aspect, the use of SMC is essential for this rotor design for two reasons: one is that the 3D nature of the flux requires isotropic material and thus excludes laminated steel; another is that the flux direction changes twice from cycle to cycle, so solid iron is not applicable because of excessive eddy current loss.

2.2.3 Stator Core Shape and Winding Area

The stator cores are alternating “C” shaped. The coil window area is designed as a rectangular shape so that it can be linearly scaled in the axial direction to accommodate required ampere-turns

at a certain current density. Also, such a shape reduces axial length compared to a circular-shape window area, which is beneficial in a wheel-hub environment that has limited width.

Because all the stator and rotor iron cores are arc-shaped, similar to a slice of pizza, to make a circular machine, the arc lengths are different at different radii, which results in varying cross-sectional areas in the stator core. Ignoring fringing and leakage, if the same amount of flux flows through the entire stator core, then higher flux density will be observed in inner radius areas and lower flux density in outer radius areas. Arguably, uniform flux density is desired in the magnetic cores to avoid early saturation and underutilization. Therefore, the stator core shape is adjusted to have decreasing thickness with increasing radius, as illustrated in Figure 2.5, thereby achieving same cross-sectional area for the flux path.

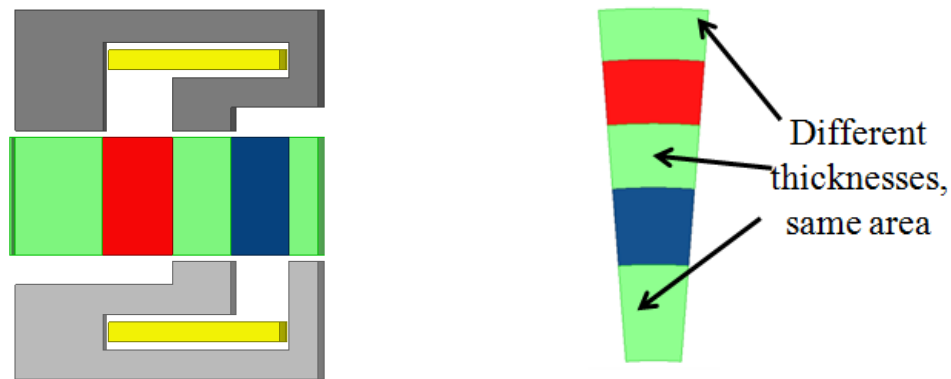


Figure 2.5. Stator shape and core area corrections.

2.3 DESIGN AND PERFORMANCE OF A TWO-PHASE MACHINE

As a proof of concept, the author decides to design the TFM into an electric scooter traction motor. Most of the electric scooters on the market have the motor mounted in the mid-hub, with multistage gearing and unreliable torque transmission to the wheel. A wheel-hub motor using direct-drive TFM would eliminate the mechanical components in a compact configuration. Besides, the scale and power rating of such a motor is more manageable as a first generation prototype.

2.3.1 Two-Phase 800-W Motor for Scooter In-Wheel Application

The TFM design targeting electric scooter in-wheel traction applications has been finalized and simulated in FEA using Flux 3D. Several practical constraints are put on the design, such as limited outer dimensions, 48-V DC bus voltage, 1 mm rotor-stator air gap, and 6 A/mm² current density, which is compatible with natural air cooling. Detailed design parameters and FEA simulated motor performances are listed in Table 2.1.

Table 2.1. Scooter Motor Design Parameters and Performances.

Pole number	30
Outer diameter (mm)	200
Inner diameter (mm)	115
Axial length (mm)	90
Weight (kg)	7.4
Coil number	15
Current RMS (A)	70
Current density (A/mm ²)	6
Coil resistance (ohm)	0.01
Electrical frequency (Hz)	75
Base speed (rpm)	300
Average torque (Nm)	26
Output power (W)	816
Estimated core loss (W)	68
Copper loss (W)	74
Efficiency (%)	85
Torque density (Nm/kg)	3.5
Torque density (Nm/L)	9.3

The space restriction in a wheel-hub environment, especially the limited axial length, dictates that only a single module with one rotor plate and two stator plates could be used; however, one module or one phase of the proposed machine has an output torque that pulsates from zero to the maximum value, which is unacceptable for traction application. To achieve ideally constant output torque, the two stator plates are physically shifted against each other at a mechanical angle that

corresponds to 90 electrical degrees, and the currents in these two coils are also phase shifted accordingly, thus creating a two-phase motor, shown in Figure 2.6.

The base speed for the designed machine is 300 rpm, which translates to 25 km/h vehicle speed. Operation at higher speeds is possible with flux weakening operation. The torque needed for an electric scooter direct-drive motor is calculated as 24 Nm to achieve 0.1g acceleration and 10% road grade.

The material for the motor iron cores is Somaloy 3P 1000 by Höganäs, with initial relative permeability of 850 and flux density of 1.63T at 10,000 A/m. The permanent magnet used in the simulation is C8 ferrite with a remnant flux density of 0.39T and relative permeability of 1.05.

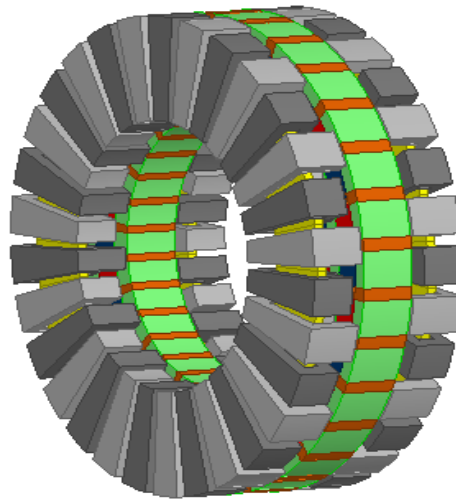


Figure 2.6. Two-phase design with shifting between stator plates.

2.3.2 No-Load Back-EMF

The no-load back-EMF plot in Figure 2.7 shows that the designed machine has a waveform closer to trapezoidal than to sinusoidal. This waveform provides a higher RMS value but requires a non-sinusoidal current to achieve a smooth torque output.

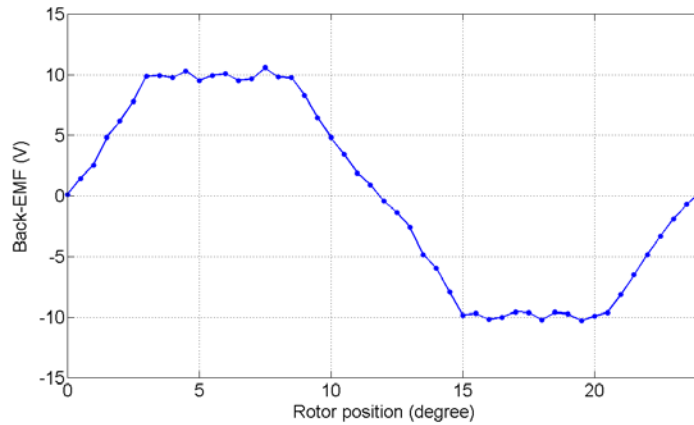


Figure 2.7. Open-circuit back-EMF.

2.3.3 Electromagnetic Torque and Cogging Torque

When driven by two-phase sinusoidal currents, the averaged output torque is 26 Nm with torque varying between 21 Nm and 30 Nm. There are two components in the torque ripple: one is electromagnetic in nature, which comes from the non-sinusoidal back-EMF waveform; another is cogging torque.

In Figure 2.8, cogging torque is shown to have an amplitude of 4 Nm which, at 15% of average torque, is a major contribution to the total torque ripple. Such large cogging torque magnitude is incompatible with the application requirement of small wind generator, because the cogging torque could potentially prevent the turbine from starting under low speed wind conditions. Because of DS-TFM's unique rotor structure, cogging torque reduction techniques developed for conventional PMSMs are not equally applicable. Further research needs to address cogging torque reduction methods that could easily apply to TFMs without adding to construction complexity.

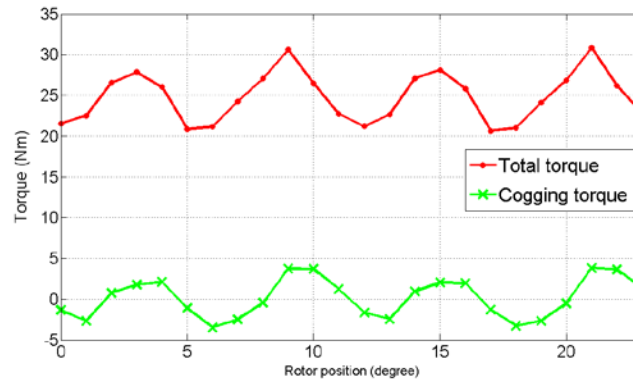


Figure 2.8. Output torque and cogging torque.

2.3.4 Torque Density

The machine active weight, which includes only permanent magnets, copper windings, and iron cores, is 7.4 kg. The cylinder volume of the TFM is 2.8 L. Therefore, the achieved torque density per weight and per volume is 3.5 Nm/kg and 9.3 Nm/L, respectively.

The achieved torque density is quite acceptable considering the use of natural air cooling for the designed current density and low-power ferrite magnets. If an advanced cooling mechanism and rare-earth magnets were to be used on the proposed machine design with further optimization, the same torque could be produced by a much smaller motor, which would result in a much higher torque density.

2.4 Core Saturation

Even though the designed DS-TFM has achieved acceptable torque density for a machine that only uses natural cooling and ferrite magnets, it suffers from severe core saturation that prevented it from fulfilling the expected level of torque. To highlight the importance of core saturation in the performance of TFMs, the Flux-Switching Transverse Flux Machine (FS-TFM) topology

described in [22] is used as a comparison machine. As summarized in Table 2.2, the FS-TFM is redesigned with the same size, material and other physical constraints as those of the DS-TFM.

Table 2.2. Summary of Parameters.

Parameters	DS-TFM	FS-TFM [22]
OD (mm)	164	164
Axial length (mm)	50	50
Magnet material	Ferrite C12	Ferrite C12
Core material	Somaloy 3P	Somaloy 3P
Rated current density (A/mm ²)	6	6
Rated current (A)	136	136
Number of turns	10	10
PM flux linkage (mWb)	9.6	7.8
Unsaturated inductance (mH)	0.49	0.15
Rated torque (Nm)	5.8	8.4

The FS-TFM has a magnetic design that utilizes all the magnets along with rotor flux concentration, but it only uses half the air gap area such that its open circuit flux linkage is inferior to that of DS-TFM. However, the DS-TFM suffers from core saturation caused by excessive armature reaction when the current loading is increased.

The effect of saturation is clearly demonstrated in the FEA simulated results in Figure 2.9(a)(b), where the inductance and torque of the DS-TFM are compared to those of the FS-TFM. Figure 2.9(a) shows that at low current loading levels, the DS-TFM has inductance that is three times higher than that of FS-TFM. As a result, when the machine's current loading is increased, excessive armature reaction flux gradually saturates the iron core, to the extent that torque production is severely limited.

The negative effects of core saturation can be clearly observed in the torque comparison plot in Figure 2.9(b), where the output torques of both DS-TFM and FS-TFM are plotted. At low current loading levels when there is no core saturation, the DS-TFM has even higher torque than the FS-TFM because of its higher PM flux linkage. However, when the currents are increased to

the rated level of 6~8 A/mm², the DS-TFM suffers from core saturation such that its torque flattens at high current loading, while the FS-TFM's torque increases almost linear with current loading.

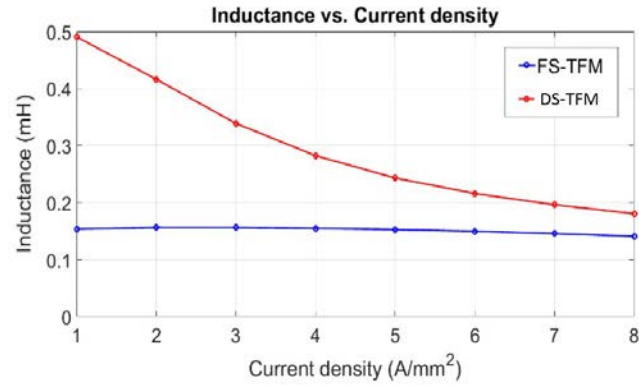


Figure 2.9. (a) DS-TFM has high inductance compared to FS-TFM.

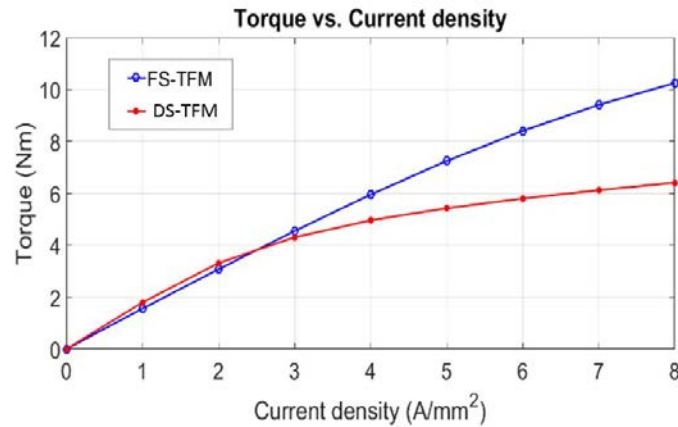


Figure 2.9. (b) Saturation of DS-TFM compared to FS-TFM.

2.5 Conclusion

The DS-TFM topology described in this chapter inherited torque production characteristics of a traditional TFM, with rotor magnetization and stator-core design innovations that address flux leakage issues faced by a TFM. This is the first TFM topology that makes full use of rotor ferrite magnets and air gap area, and totally eliminated rotor flux leakage. The fundamental understanding gained on leakage-proof rotor design provides valuable guidance to future variations of TFM

topology. The design of a scooter wheel-hub motor shows promising performance in terms of torque density. However, the current design is plagued by high torque ripple and excessive core saturation. Further improvements in those areas are required in order to satisfy the application needs. The high inductance of DS-TFM leads to the important fundamental study in the next chapter.

CHAPTER 3 INDUCTANCE ANALYSIS OF TFM

Inductance is an important parameter in an electric machine's equivalent circuit model. For any PMSM, a reasonable amount of inductance is essential for current control and field weakening operation. An IPM also makes use of saliency in dq inductance for reluctance torque. In designing conventional PMSM, the concern is usually about not having enough inductance, because the permanent magnets act as large air gap that reduces inductance.

For TFM, however, the designer often struggles with the inductance being too high. A high inductance in TFM not only causes low power factor and core saturation, but also leads to reduced efficiency and torque output. High inductance has become the single most important obstacle that prevents TFM from realizing its full potential.

3.1 Saturation and Low Power Factor: the Issues with TFM Inductance

3.1.1 Relationship between armature inductance, rotor flux linkage, and power factor

The vector diagrams in Figure 3.1(a)(b) explain the relationship between inductance, flux linkage and power factor for conventional PMSM and PM-TFM, respectively.

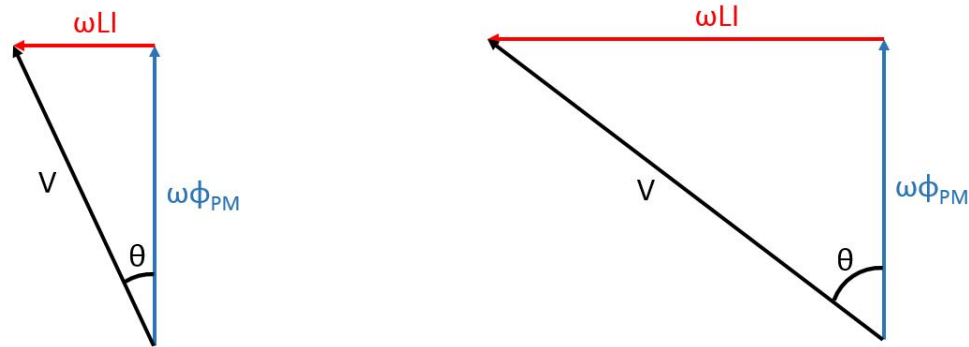


Figure 3.1. (a) Typical PMSM power factor. Figure 3.1. (b) Typical TFM power factor.

The two machines have the same magnitude of stator current that is aligned with the q-axis, with the only difference between the two being the amplitudes of armature inductance. We ignore resistive voltage drop, then the equation below calculate power factor as:

$$\cos\left(\tan^{-1}\frac{LI}{\phi_{PM}}\right) \quad (1)$$

$$\cos\left(\tan^{-1}\frac{XI}{E}\right) \quad (2)$$

The power factor is clearly determined by the ratio of armature reaction flux and rotor flux linkage. For PMSM, because it usually has relatively low armature flux compared to rotor flux linkage, its power factor is typically high. For TFM, whose armature flux can be several times higher than the rotor flux linkage, its power factor can fall into the range of 0.35~0.55 [14].

3.1.2 Negative effects of high inductance

Earlier versions of TFMs, as those reported in [1][2][12], suffer from low power factor primarily because the rotor magnets are not fully utilized, which leads to insufficient flux linkage. The DS-TFM topology of chapter one, in deploying alternating C-core design, successfully eliminated rotor flux leakage and doubled rotor flux linkage. However, the DS-TFM still suffers from low power factor, because in using the extra stator cores, it also almost doubled the armature inductance. As a result, according to Eq. (1), the power factor only saw marginal improvement if there is any. All the negative effects of high inductance can be summarized below:

- Low power factor adds to cost of inverter
- Limited torque output because of saturation
- Extra core loss from high flux density
- Distorted waveform due to saturation

3.1.3 Inductance study towards a solution

Previous research efforts have been made to accurately model the inductance and power factor of TFM either through magnetic equivalent circuit [23] or through FEA modeling [20]. But few research offers in depth study on the fundamental reason for TFM's high inductance, and there has been no methodology proposed or developed for the design of TFM that is optimized for reduced inductance and improved power factor. In this chapter, a comprehensive study is conducted, both qualitatively and quantitatively, not only on modeling the TFM's inductance, but more importantly on ways to lower its inductance.

3.2 TFM'S Inductance is Fundamentally Different

TFM shares several common features with 1-slot-per-pole Fractional Slot Concentrated Winding (FSCW) PMSM [24], such as concentrated winding and segmented core structure. Yet, in terms of torque production and inductance, TFM's unique winding configuration makes it fundamentally different from that of a radial flux PMSM. Table 3.1 provides a comparison between a TFM and a PMSM designed with the same pole number, air gap area, air gap flux density, air gap length, and number of turns.

Because TFM can avoid the competition between magnetic and electric loading by allowing its entire winding to link all the stator poles, its number of turns per pole pair equals to the total number of turns N , while PMSM's total conductor turns are divided among the pole pairs to give the number of turns per pole to be N/P . Consequently, the TFM has a PM flux linkage that is P times larger and an inductance that is P^2 times larger than those of PMSM. When excited with the same phase current I , TFM exhibits much higher torque density than PMSM, but suffers from a much higher armature flux and lower power factor, both because of the same reason.

Table 3.1. Compare TFM and FSCW PMSM.

Design Variables	TFM	FSCW PMSM
Total number of turns	N	N
Phase current	I	I
Pole pair number	P	P
Air gap length	g	g
Air gap area	A	A
Air gap flux density	B	B
Turns per pole pair	N	N/P
Permeance P_m	$\mu A/g$	$\mu A/g$
PM flux linkage	NBA	NBA/P
Torque	$NIBA * P$	$NIBA$
Inductance	$N^2 P_m$	$(N/P)^2 P_m$
Power factor	$\cos \left(\tan^{-1} \frac{NP_m I}{BA} \right)$	$\cos \left(\tan^{-1} \frac{NP_m I}{PBA} \right)$

3.3 Inductance Analytical Equations and Design Guidelines

This chapter uses the basic surface Permanent Magnet (PM) TFM [12] as the example topology for analysis, which is illustrated in Figure 3.1(a). The basic TFM topology has C-shaped core for each stator pole pair, and surface magnet pairs attached to the rotor back iron and magnetized radially. The same analysis approach is equally applicable to other TFM topologies. The geometry being considered for analytical inductance expressions is one pole pair of a rotational TFM that is simplified as a linear motor. In deriving the inductance expressions using basic magnetic circuit theory, it is assumed that the permeability of iron is infinite, and that the permeability of the PMs is the same as that of air. The purpose of using these expressions is more to identify the key geometric parameters that affect the inductance rather than to model the inductance values accurately.

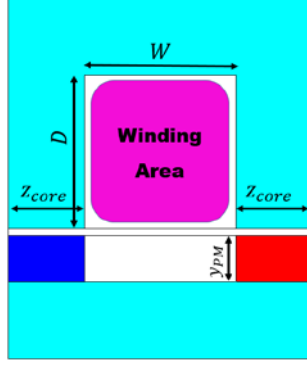
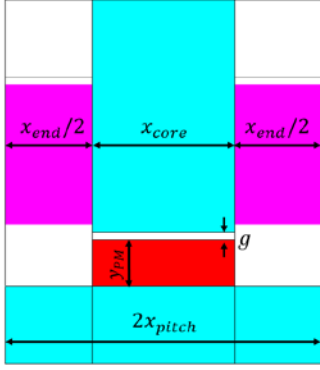


Figure 3.2. (a) Front and side view of basic TFM topology.

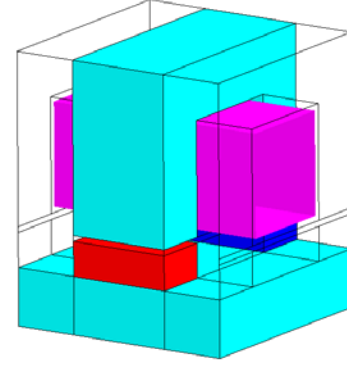


Figure 3.2. (b) Basic TFM topology modeled in 3D FEA.

The modeling approach categorizes TFM's inductance into four components: air gap inductance, slot leakage inductance, end winding inductance, and fringing inductance. Even though the total armature flux determines the power factor, and hence, it is not absolutely necessary to separate different inductance components, doing so is helpful in gaining insightful understanding of how each component could be reduced through design improvements.

3.3.1 Air gap inductance

Air gap inductance [25] whose flux path crosses the air gap and links with the rotor back iron is calculated as

$$L_{airgap} = N^2 \mu_0 \frac{K_s \cdot x_{pitch} \cdot z_{core}}{2(g + y_{PM}) \cdot C_s} \quad (3)$$

where N is the number of turns, and C_s is Carter's coefficient given by

$$C_s = \frac{x_{end} + x_{core}}{x_{core} + \frac{4g}{\pi} \ln\left(1 + \frac{\pi x_{end}}{4g}\right)} \quad (4)$$

In the above equations, core span-factor K_s is defined as $K_s = \frac{x_{core}}{x_{pitch}}$ to denote the ratio of core width to pitch width. K_s and PM thickness y_{PM} are the two main parameters that affect air gap inductance.

In order to reduce the air gap inductance component, K_s should be reduced to have less winding covered by iron core. However, the air gap flux shares the same magnetic path as the useful flux linkage from the rotor surface permanent magnets, such that any reduction of inductance by reducing pitch width will also incur reduction in PM flux linkage. This conflict demands magnetic circuit design that utilizes flux concentration in which PM flux linkage is less sensitive to pitch width.

Another approach is to increase the thickness of the PMs, which are in the flux path and act as lengthened air gap that reduces inductance. This alternative also slightly boosts PM flux linkage, but comes at the expense of more magnet material; hence, the approach is more suitable to be adopted with non-rare earth magnets.

3.3.2 Slot leakage inductance

Slot leakage inductance [25], whose flux path follows the stator C-core and closes around the slot opening, similar to the case in FSCW PMSM, is calculated as:

$$L_{slot} = N^2 \mu_0 x_{core} \frac{D}{3W} \quad (5)$$

The above equation show that the slot dimension affects the slot inductance. For conventional radial flux slotted machines, multiple slots and teeth share the available circumferential space within the stator, such that the width of the slot is severely constrained. However, in the case of TFM, the width of the single slot extends in the axial direction. Therefore, for the same slot winding area, the designer has more flexibility to choose wider but shallower slots to reduce slot leakage inductance.

3.3.3 End winding inductance

End winding inductance [25] is flux path is completely through air, which corresponds to the winding section that is exposed in air between stator poles. End winding inductance is inversely proportional to the pitch factor K_s , and is calculated as:

$$L_{end} = N^2 \mu_0 \frac{x_{end}}{2\pi} \ln\left(\frac{R}{r}\right) \quad (6)$$

where R is the outer radius of the end winding area, r is the inner radius of the end winding area. Because the end winding flux path is totally in the air, this inductance component is only a very small portion of the total inductance.

3.3.4 Fringing inductance

Fringing inductance, whose flux path occupies the same air space as the end winding flux, but is due to the contribution from fringing flux that enters inter-polar air gap from the sidewalls of the stator cores. This inductance component is unique to TFM, whose many iron cores have side-faces exposed to air, where magnetic flux escapes from the iron core and fringes into the space surrounding the end winding. The prevalence of fringing flux highly depends on the number of stator core side-faces.

Deriving an analytical expression for fringing inductance is quite difficult, but its magnitude for one pole pair should remain relatively constant, as is shown later through 3-D FEA simulation. Its expression can be simplified as a constant fringing-flux per-pole-pair L_{fringe} , pole times the number of pole pairs as in (7).

$$L_{fringe,total} = P * L_{fringe,pole} \quad (7)$$

Consequently, a high pole number TFM would see fringing inductance making up a major portion of its total inductance. Even though increasing the pole number would theoretically

produce proportionately higher torque, the extra fringing flux that accompanies will cause stator core saturation, which is one of the factors that eventually limit the available torque.

3.3.5 Total inductance and power factor

The above way of separating the inductance into individual components is only to help with the analytical equation derivation and conceptual understanding. In the end, it is the total inductance L_{total} , which is the summation of all the inductance components that determines the TFM's armature reaction and power factor. Large inductance not only leads to poor power factor, but also causes excessive armature reaction that result in core saturation and limited torque production.

If the stator resistance is ignored, the TFM's power factor is determined by the ratio of armature reaction flux and PM flux linkage, and is shown in Eq. (8).

$$Power\ factor = \cos\left(\tan^{-1}\left(\frac{L_{total} \cdot I}{\lambda_{PM}}\right)\right) \quad (8)$$

where λ_{PM} is the PM flux linkage, and I is the stator current. To design a TFM with improved power factor, the target is to reduce the inductance as much as possible without negatively affecting PM flux linkage at the same time.

3.4 Verification by 3D FEA Simulation

In order to verify the trends summarized from the theoretical equations above, the basic TFM topology is modeled in Flux3D for FEA simulation, as shown in Figure 3.2(b). Various inductance components are separated by calculating the stored energy in the corresponding volume area when constant current is passed through the conductors. The resultant inductance values are compared with analytical calculations when key geometric parameters are varied.

3.4.1 Simulation Method

The methods to separate the different inductances in an electromagnetic circuit using FEA based simulation have been adopted from those described in [26]. The FEA software Flux3D calculate the stored magnetic energy W by integrating $B \cdot H$ in the volume regions that correspond to individual inductance components. The method uses magneto-static analysis by conducting a constant current through the winding conductors which gives the inductance component as:

$$L = \frac{2W}{I^2} \quad (9)$$

The problem is then to determine which energy to use for the target inductance component. Figure 3.3 illustrates the volume regions of the TFM that offer the magnetic energy for inductance calculation, as well as flux lines that corresponds to the inductance. The PMs are “turned off”, as they behave the same as air volumes for inductance calculation.

Slot leakage flux, end winding flux, and fringing flux exist even when the rotor is absent. The energy for slot leakage flux, as illustrated in Figure 3.3(a), is calculated in volume regions surrounding the slot windings, which include stator iron, slot, PMs and air gap.

The energy for end winding flux and fringing flux is stored in the air volume surrounding the end winding part, as shown in Figure 3.3(b). The separation of end winding inductance and fringing inductance is achieved by sweeping design parameter K_s , based on the assumption that fringing inductance is independent of K_s , while end winding inductance is proportional to $(1-K_s)$. This relationship is expressed in Eq. (10).

$$L_{air} = L_{end} * (1 - K_s) + L_{fringe} \quad (10)$$

Airgap flux is defined as the armature flux that links with the rotor back iron such that it only exists when rotor is present, as illustrated in Figure 3.3(c) and 3(d). Compared to the above case when the rotor is absent, the additional magnetic energy stored in the volume regions in this case is the amount that corresponds to airgap flux.

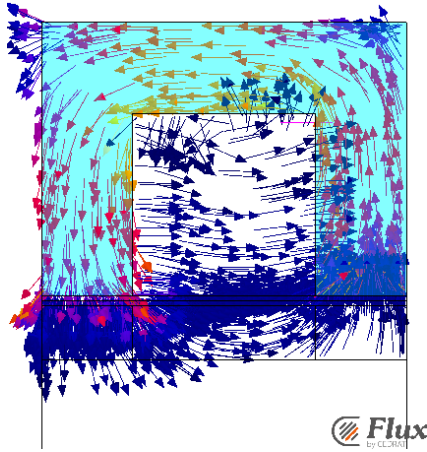


Figure 3.3. (a) Slot leakage flux.

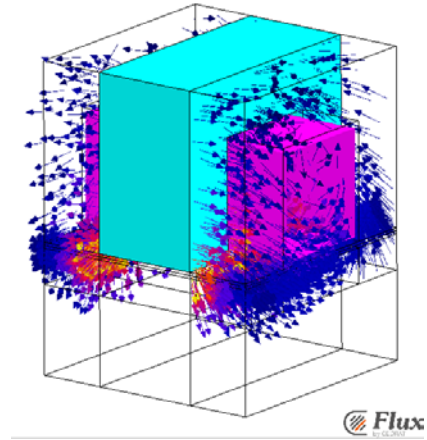


Figure 3.3. (b) End winding flux and fringing flux.

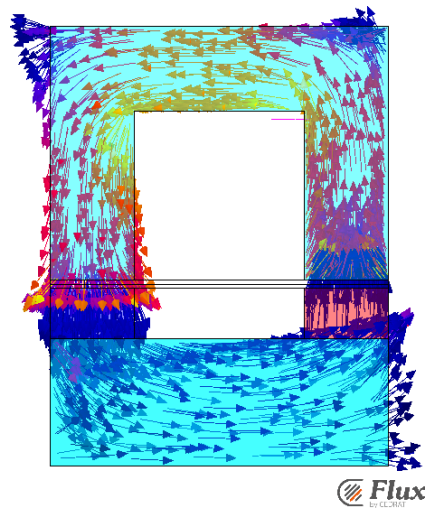


Figure 3.3. (c) Air gap flux.

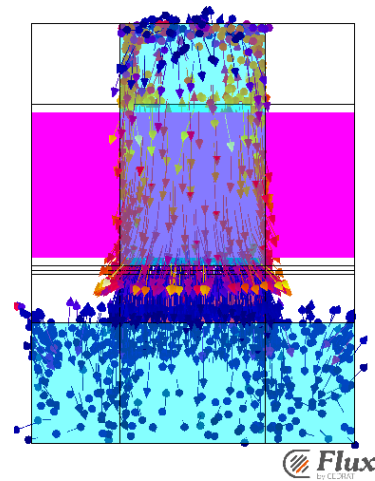


Figure 3.3. (d) Air gap flux.

3.4.2 Simulation Results

The key geometric parameters that determine the inductance values have been identified in earlier in this chapter for each inductance component. In Figure 3.4, the values of each inductance component from both analytical expression and FEA simulation are plotted together while the corresponding key geometric parameter is varied. Note that in Figure 3.4(d), the fringing inductance component is only available through FEA.

Even though noticeable differences exist between inductance values from the two modeling methods, the discrepancies are expected because the ideal analytical expressions ignored nonlinearity and 3D flux paths, while the FEA simulation reflects the physical reality. Nonetheless, the FEA simulation successfully verifies the trends observed from analytical expressions, which serve as the guideline in proposing design methods that reduce inductance and improve the power factor for TFM.

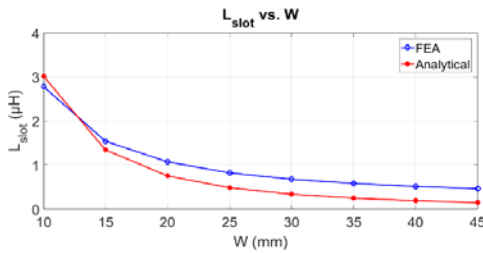


Figure 3.4. (a) Slot leakage inductance with respect to width of slot W .

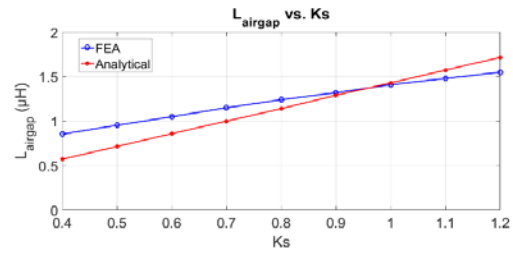


Figure 3.4. (b) Air gap inductance with respect to pitch factor K_s .

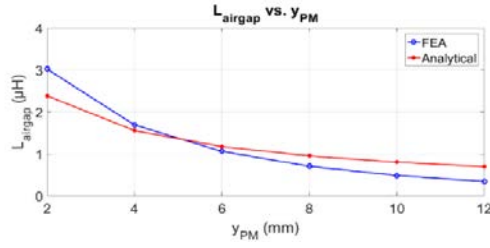


Figure 3.4. (c) Air gap inductance with respect to magnet thickness y_{PM} .

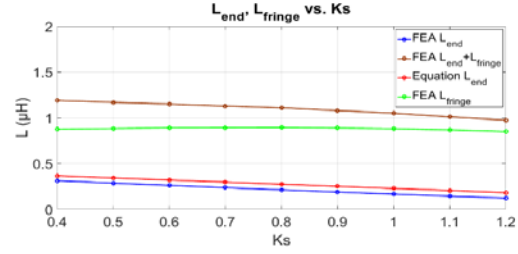


Figure 3.4. (d) End winding and fringing inductance with respect to K_s .

Figure 3.5 shows the reduction in total inductance with respect to decreasing pitch width factor K_s . This is because major portion of the total inductance, which comes from the slot leakage inductance and air gap inductance, is proportional to K_s , while only a relatively smaller portion of end winding inductance is proportional to $(1-K_s)$. Therefore, a better approach to reduce overall inductance is to select a possible smaller K_s value under the condition that PM flux will not be negatively affected.

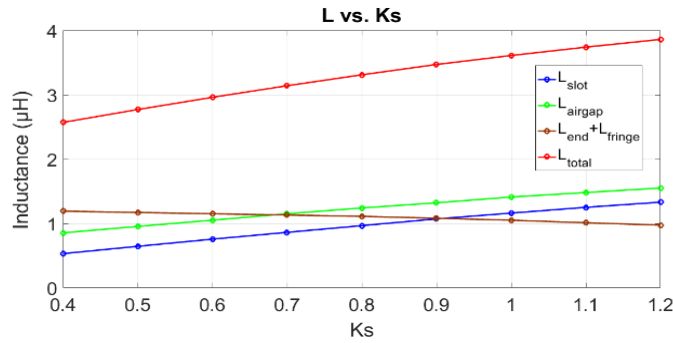


Figure 3.5. Total inductance with respect to K_s .

3.5 Conclusion

This chapter's study helped to gain deeper understanding of the TFM's inductance and power factor from a fundamental and physical perspective, and concluded that TFM has an unavoidably

high inductance, because the winding of TFM links with all the stator poles, which is the also the contributing factor for TFM's high torque density.

By separating total inductance into individual components based on distinct flux paths, the proposed magnetic circuit model linked each inductance component to key geometric parameters. Design guidelines are then proposed and verified as a solution to reduce TFM's inductance and minimize the inherent saturation problem. The design methods are then used in the next chapter to design a novel FS-TFM with reduced inductance and improved power factor.

CHAPTER 4 STATOR-PM TRANSVERSE FLUX MACHINE

This chapter aims to design the best possible TFM targeting direct drive application, under the constraints of using non-rare-earth magnets, natural air cooling, and structural modularity. The Stator-PM TFM, or Flux Switching TFM, built upon the lessons learned from the DS-TFM in Chapter 2, and designed following the guidelines summarized from the inductance study in Chapter 3, is the thesis' proposed best possible solution to the target applications. Besides the basic application requirements, the new design also strives to incorporate the following features:

- **Flux focusing capability:** To be compatible with using low energy density non-rare-earth magnets, but still achieves high air gap flux density. Either ferrite or AlNiCo magnet offers low cost, low loss, and is more resistant to temperature variation.
- **Balanced performance:** Electric machine design is a typical multi-objective multi-variable optimization problem, involving inevitable trade-offs among performance criteria including torque density, efficiency, power factor and torque ripple. A good design should not overly sacrifice performance in one aspect in order to boost the others.
- **Structurally and thermally robust:** Vast majority of motors adopt radial air gap, outer stator and inner rotor construction, mostly because of structural and thermal benefits. Other configurations, such as axial air gap or outer rotor, require special axial loading bearings, and pose extra challenge in designing supporting structure. Inner stator severely hampers heat dissipation from stator copper loss.
- **Convenient for mass production:** Stator core, rotor core and magnets should maintain modularity, which benefits manufacturing and maintenance. Winding construction and insertion, which incurs major labor cost in conventional machines, should be easily automated, utilizing TFM's unique concentrated toroidal winding.

4.1 Stator-PM TFM Topology

Using ferrite magnets in any TFM topology is challenging, because the low residual flux density of ferrite magnets requires a magnetic circuit design with flux focusing. Radial-flux PMSMs with ferrite magnets usually adopt the spoke-type rotor design to obtain maximum flux focusing. However, this approach either requires “bridges” that introduce undesirable leakage flux paths but are essential for structural integrity, or requires a segmented rotor that is structurally demanding [27]. Furthermore, TFM usually has very high pole number, which leaves little space in each rotor pole for magnet placement. The TFM topology in [9] utilized flux focusing with NdFeB magnets, but the flux focusing factor is not large enough for ferrite magnets, and the segmented outer rotor lacks structural robustness. To solve the above issues related to ferrite magnet machines, the Flux Switching PM machines (FS-PMSM) [28] serve as an inspiration for the proposed Stator-PM TFM. Stator-PM TFM in Figure 4.1 is able to offer superior magnetic design without sacrificing structural integrity, because the stator allows more space for PM placement, and thus, more freedom in magnetic circuit design that focuses PM’s flux into the air gap. Also, segmentation in the stator and solidity in the rotor is structurally preferable than the opposite case.

Figure 4.2 illustrates one pole pair of the proposed Stator-PM TFM, together with PM magnetization and flux paths. C-shaped stator pole pieces wrap around the phase winding, which is a ring-shaped concentrated winding whose construction can be easily automated. Ferrite magnets are sandwiched between stator cores of each pole, and circumferentially magnetized with alternating polarities, shown red and blue in the figure. The inner rotor is one solid structure with salient tooth in each pole. The two opposing magnets’ flux enters the stator pole piece, and focuses into the air gap where it links with the rotor and loops back to the PMs through adjacent stator

poles. The flux linkage would reverse polarity once the rotor rotates 180 electrical degrees. Because of the three-dimensional nature of TFM's flux path, isotropic Soft Magnetic Composite (SMC) material [29] is used for both stator and rotor iron.

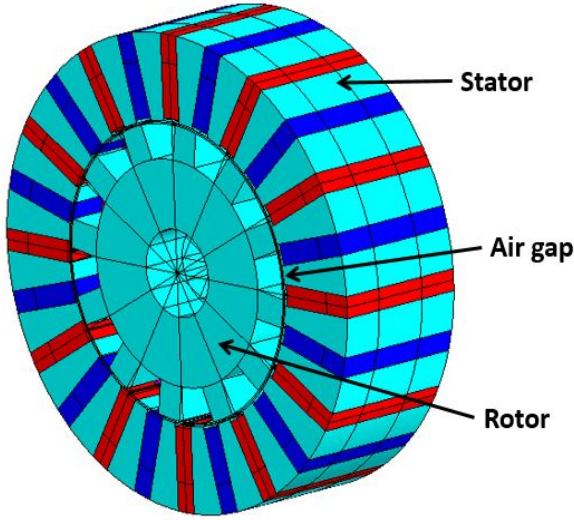


Figure 4.1. Stator-PM TFM topology.

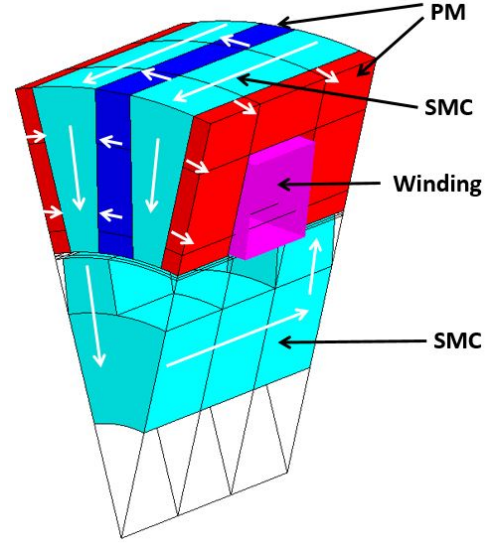


Figure 4.2. Stator-PM TFM flux path.

4.2 Design and Optimization with 3D FEA

A one horsepower Stator-PM TFM is designed as a direct drive traction motor for electric scooters. Because of the identical and independent nature of TFM's phases, only one phase module of the traction motor is modeled and simulated using Flux3D FEA software. A three-phase Stator-PM TFM would be axial stacking of three 120-degree-shifted single-phase modules. Table 4.1 summarizes the design parameters, material properties, and simulated performance at rated condition.

In order to facilitate prototype construction, the standard NEMA 143T aluminum frame from a commercially available one horsepower induction motor is to be reused as the Stator-PM TFM housing. The outer diameter and axial length of the magnetic active parts are limited to 154 mm and 50 mm respectively to fit into the frame. At rated torque, the current density in the conductor

is 5 A/mm^2 assuming Totally Enclosed Non-Ventilated (TENV) cooling condition. The actual currents for continuous torque and peak torque currents depends on heat-run temperature to be measured on the prototype motor.

Table 4.1. List of Single Phase Stator-PM TFM Design Parameters and Values.

Parameters	Values	Units
OD (mm)	154	mm
Axial length (mm)	50	mm
PM residual flux density (T)	0.4	T
PM intrinsic coercivity (kA/m)	318	kA/m
SMC max relative permeability	430	
SMC flux density at 10 kA/m (T)	1.46	T
Current density (A/mm^2)	5	A/mm^2
Stator MMF (Ampere turns)	1575	Ampere turns
Rated speed (rpm)	300	rpm
Rated torque (Nm)	7.2	Nm
Output power (W)	226	W
Power factor	33	%
Efficiency	78.6	%
Core loss (W)	14.6	W
Copper loss (W)	46.9	W
PM weight (kg)	0.98	kg
Iron weight (kg)	1.93	kg
Copper weight (kg)	1.01	kg

4.2.1 Torque, Efficiency and Power Factor

According to [12][14], TFMs utilizing NdFeB magnets suffer from low power factor (0.35~0.55) and magnetic saturation because of high leakage inductance and excessive armature reaction. Ferrite magnet based TFMs are especially susceptible to low power factor because of low magnetic loading. The Stator-PM TFM topology boosts the PM flux linkage while simultaneously lowering the inductance which reduces the saturation effect from armature reaction.

TFMs usually have great potential to be designed for very high rated torque. However, pushing for extreme torque output should not come at the cost of efficiency and power factor. Figure 4.3 explains the deliberation in determining the machine's rated torque level. The blue curve in Figure

4.3(a) shows the output torque of Stator-PM TFM using Somaloy Prototyping Material, while Figure 4.3(b) shows its efficiency and power factor when the winding current density is increased from 0 to 8 A/mm². The red curve in Figure 4.3(a) represents the case when an ideal linear iron material is used. Compared to the case without saturation, the iron core of Stator-PM TFM is right at the onset of saturation when operated at the rated torque with the continuous operating current density of 5 A/mm². Taking into consideration the combined trends shown in Figure 4.3, further increase in current density would incur too much penalty in power factor and efficiency, which cannot be justified by only moderate increase in torque output. The final Stator-PM TFM design has an appropriate compromise among torque, efficiency, and power factor to deliver a well-balanced performance.

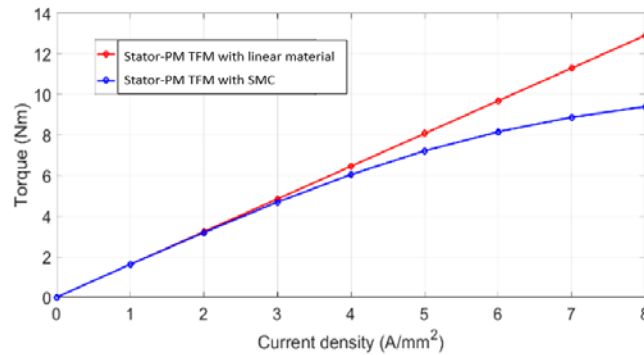


Figure 4.3. (a) Torque vs. current density.

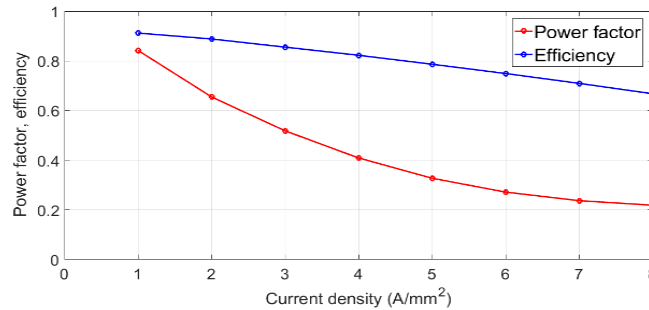


Figure 4.3. (b) Power factor, efficiency vs. current density.

4.2.2 Cogging Torque

TFMs usually have high torque ripple because its rotor and stator are doubly salient with the same number of teeth. Out of the numerous methods in reducing cogging torque of PMSMs, the “magnet spacing” approach in [30] is particularly suitable to reduce certain harmonic numbers in the cogging torque. Successful implementations of this method include the axial flux PMSM in [31] as well as the “tooth pitching” method in [32] on stator teeth of a rotor-PM TFM.

In this research, a similar “tooth pitching” method is applied to the rotor teeth of the Stator-PM TFM, as shown in Figure 4.4(a). Without compromising the simplicity of rotor construction, every other rotor tooth is rotated by 30 electrical degrees to eliminate the dominant 6th order harmonic in cogging torque. The simulation result in Figure 4.4(b) shows three-phase cogging torque is 2.21 Nm with full pitch, and is reduced to 0.17 Nm after tooth pitching. When operating at rated current, the three-phase total torque ripple is 3.3%, as shown in Figure 4.4(c). Because of pitching of the rotor teeth, the Stator-PM TFM suffers a 7% reduction in average torque, which is justifiable considering the significant reduction in torque ripple. However, it is noteworthy that in a prototype motor or in a production motor, the effectiveness of this method is subject to manufacturing tolerances.

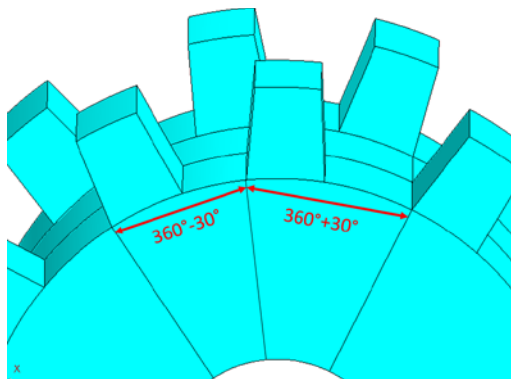


Figure 4.4. (a) Rotor tooth pitching shown in electrical degrees.

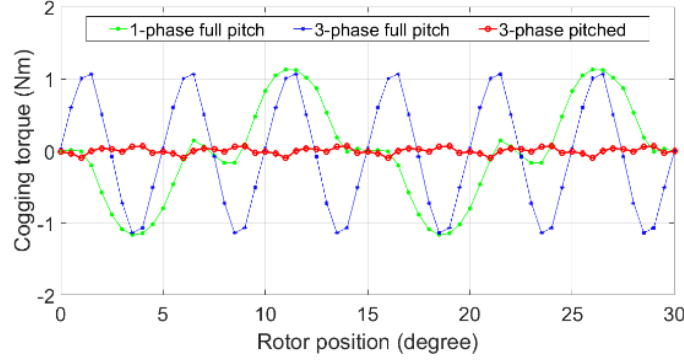


Figure 4.4. (b) Cogging torque.

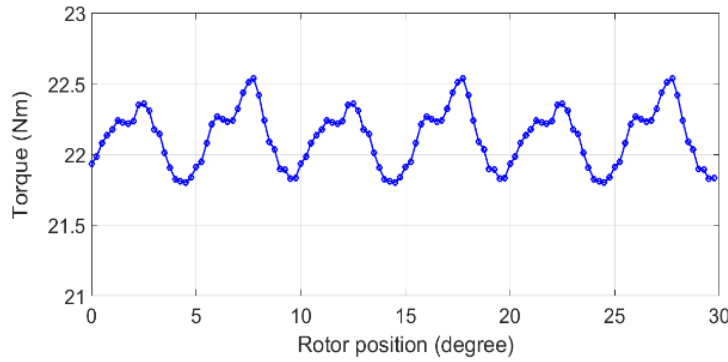


Figure 4.4. (c) Three-phase torque ripple.

4.2.3 PM Demagnetization of Stator-PM TFM

Ferrite magnets are especially susceptible to permanent demagnetization from armature field, because of their low intrinsic coercivity. The design of Stator-PM TFM entails two features that protect the magnets from demagnetization. One feature is the large magnet thickness (7.45 mm). The other feature being that the major armature flux path of Stator-PM TFM is perpendicular to the anisotropic magnetization direction of the PMs.

In order to evaluate under which rotor position the PMs are most susceptible to demagnetization, rated current are applied when the rotor teeth either align with the stator teeth which corresponds to d-axis current, or align with the PMs which corresponds to q-axis current. The PMs are set as air region in 3D FEA simulation to show only the armature flux path in the above two cases, as shown in Figure 4.5(a) and (b). For both cases, a very small portion at the

lower corner of the magnets, where the armature reaction flux goes against the magnetization direction of the PMs, are at risk of partial demagnetization, as shown in Figure 4.5(c). To reduce this potential risk, length of the magnets has been reduced by 1 mm in the Stator-PM TFM prototype to minimize the demagnetization region.

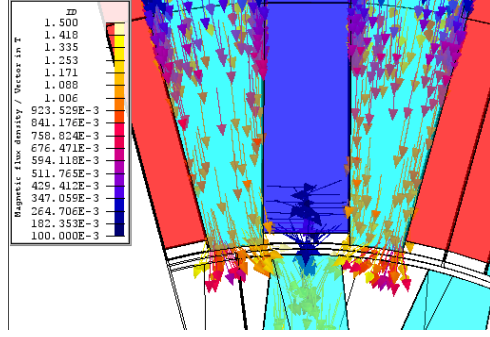


Figure 4.5. (a) Armature flux with q -axis current.

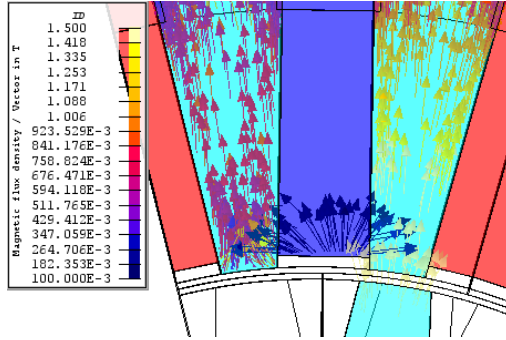


Figure 4.5. (b) Armature flux with d -axis current.

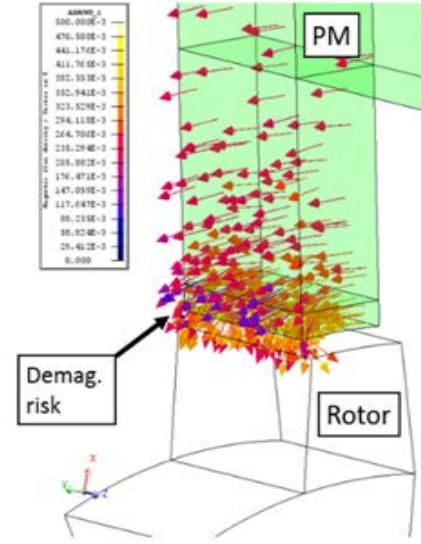


Figure 4.5. (c) Flux in PM region.

Further study evaluates to what extent the demagnetization risk affects the machine performance. Figure 4.6(a, b, c, d) shows the flux density of the PMs before and after demagnetization under various loading conditions. At the same lower corners of the magnets, flux density are reduced to almost zero, suggesting various extents of permanent demagnetization. This result is consistent with conclusions from [33] pertaining to demagnetization study on a similarly structured radial flux FS-PMSM.

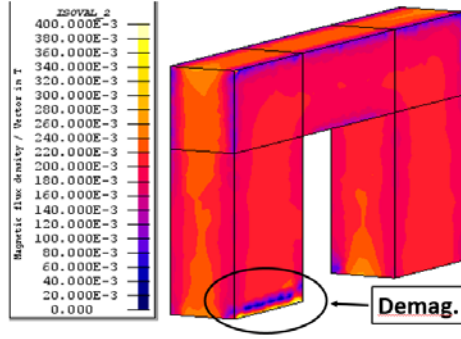


Figure 4.6. (a) PM flux density after peak q -axis current.

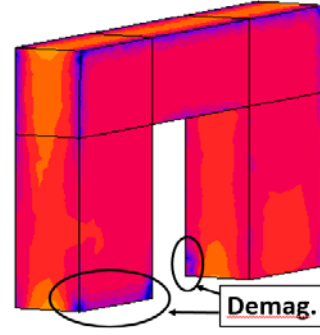


Figure 4.6. (b) PM flux density after peak d -axis current.

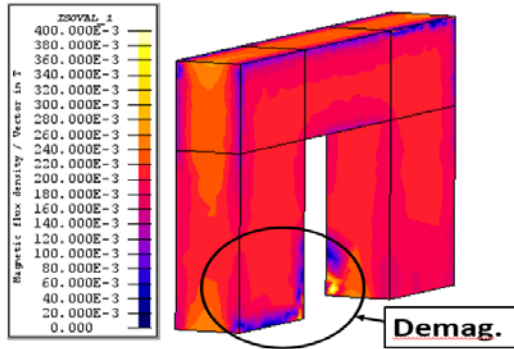


Figure 4.6. (c) PM flux density after ten times peak q -axis current.

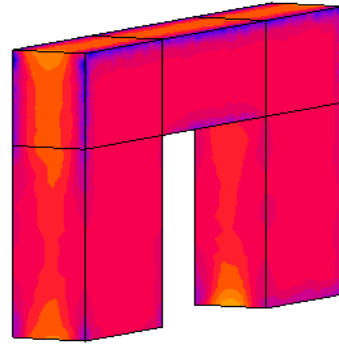


Figure 4.6. (d) PM flux density before current loading.

The effect of the demagnetization is very limited since the affected area represents only a very small portion of the total magnet volume. Figure 4.7(a) and (b) show almost identical open circuit flux linkage and torque output before and after the demagnetization. Closer examination of the results show that the reduction in peak flux linkage and average torque are within 1%.

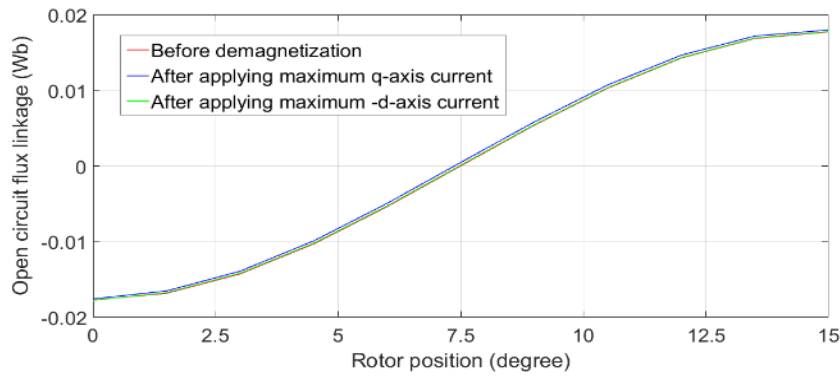


Figure 4.7. (a) Open circuit flux linkage before and after demagnetization.

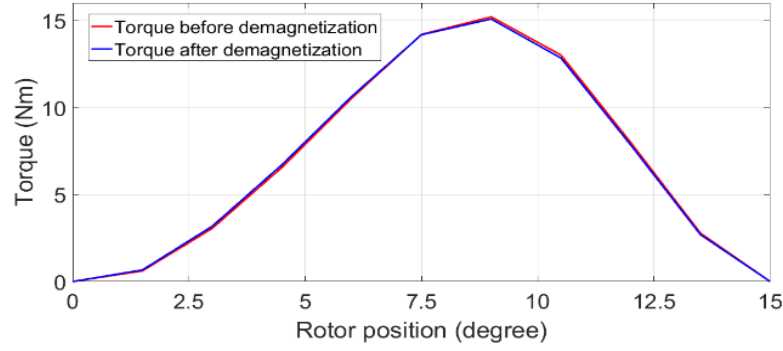


Figure 4.7. (b) Electromagnetic torque before and after demagnetization.

4.2.4 Constant Power Speed Range

Having an extended constant power speed range is an indispensable feature for motors used in vehicle traction applications. Even though TFM has the same equivalent electrical circuit model as a regular non-salient PMSM, its extremely high inductance makes the field weakening operation special. For the designed Stator-PM TFM with ferrite magnets, its weak magnetic loading and high inductance result in a very small characteristic current. Based on Stator-PM TFM's open circuit flux linkage and d-axis inductance, the characteristic current is calculated as:

$$I_c = \frac{\lambda_{PM}}{L_s} = \frac{12.6 \text{ mWh}}{0.8 \text{ mH}} = 15.7 \text{ A} \quad (1)$$

which is much smaller than the machine's rated current, and requires only 12.8 degree current advance angle when operating at the maximum current limit.

In this sense, the Stator-PM TFM would be considered an "infinite drive system," in which very little current is needed in the negative d-axis to totally cancel out the PM flux linkage. However, this field weakening operation only marginally increases the machine speed beyond the base speed, because in such low power factor machines, armature inductive voltage composes the majority of the terminal phase voltage. Further extension of the constant power speed range would

require the q-axis current magnitude to reduce, while maintaining the -15.7A d-axis field weakening current.

The infinite drive system field weakening operation is illustrated in Figure 4.8(a), where point A represents the base speed, point B represents maximum weakening of PM's field at rated current, and point C to E represents extended speeds with reduced current magnitude. The corresponding operating points in Figure 4.8(a) have been simulated in Flux3D assuming the TFM is operated under the constraints of three-phase inverter with 48V dc bus voltage, 50 A per phase current limit, and 300 rpm base speed. Figure 4.8(b) plots the Stator-PM TFM's torque speed curve and constant power speed range up to 3 times base speed. Points A to E in Figure 4.8(b) are marked to correspond to the operating conditions in Figure 4.8(a). The machine power at higher speeds are slightly higher than the base speed power, because the stator cores have less saturation with reduced armature reaction, thereby providing more torque per unit current. Further speed increase is possible, but will be limited by practical factors such as mechanical constraints and excessive core loss.

The fact that Stator-PM TFM having high leakage inductance is beneficial in two ways regarding the extended speed range. On one hand, the low field weakening current because of the high inductance greatly boosts machine efficiency at high speed, as will be shown in the next section. On the other hand, the field weakening flux follows the leakage flux path, thereby avoids demagnetization of the permanent magnets. The combination of those features make Stator-PM TFM superior to surface magnet PMSM for vehicle traction applications.

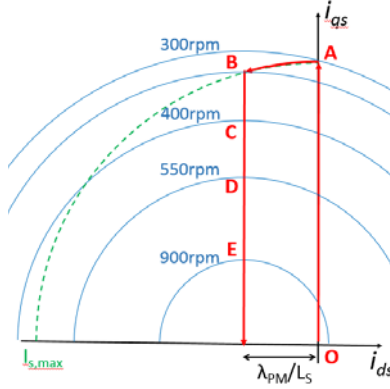


Figure 4.8. (a) Infinite drive system constant power operation.

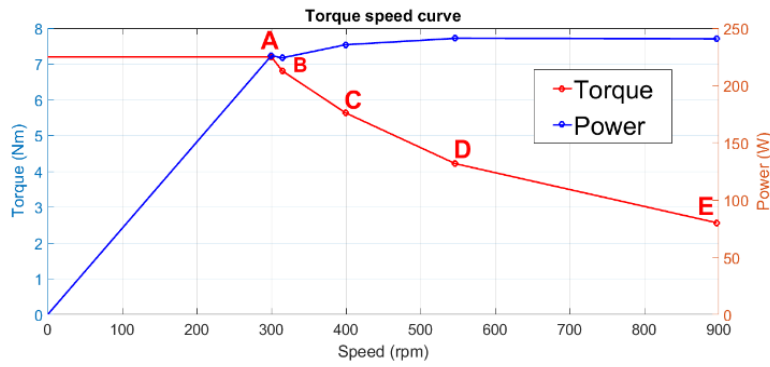


Figure 4.8. (b) Stator-PM TFM torque speed curve and constant power speed range.

4.2.5 Efficiency Map for Entire Operating Region

Loss components for the Stator-PM TFM include stator copper loss, and stator and rotor core loss. There is no magnet loss because ferrite magnets are non-conductive. Friction and windage loss are ignored because the machine operates at very low speed.

The stator winding has 30 turns per phase and 10.5 mm^2 cross section area per turn, and has a $17 \text{ m}\Omega$ per phase resistance at room temperature. For efficiency estimation, the stator copper loss is easily calculated based on phase current magnitude and phase resistance.

Core loss for the SMC material is calculated using the same Bertotti method as that used for laminated steel core loss estimation. Equation (2) below is used together with 3D FEA to calculate the average core loss in one electrical cycle. The material supplier datasheet [29] has provided the

hysteresis coefficient K_h , eddy current coefficient K_{ep} , and other parameters for the Bertotti equation.

$$P_{core} = K_h \cdot f \cdot B^{1.75} + K_{ep} \cdot f^2 \cdot B^2 + \frac{f^2 \cdot B^2 \cdot d^2}{1.8 \cdot \rho \cdot \sigma \cdot 1000} \quad (2)$$

With both copper loss and core loss calculated, together with the field weakening strategy described in the previous section, the efficiency map for Stator-PM TFM is plotted for the entire operating range except for extremely low speed and low torque regions, as shown in Figure 4.9. From the efficiency map, it is observed that the Stator-PM TFM has above 90% efficiency in the medium-speed to high-speed low-torque region, where electric vehicles operate most of the time [31]. This is made possible by Stator-PM TFM's low current magnitude during field weakening, and by SMC's relatively low eddy current loss at high frequencies.

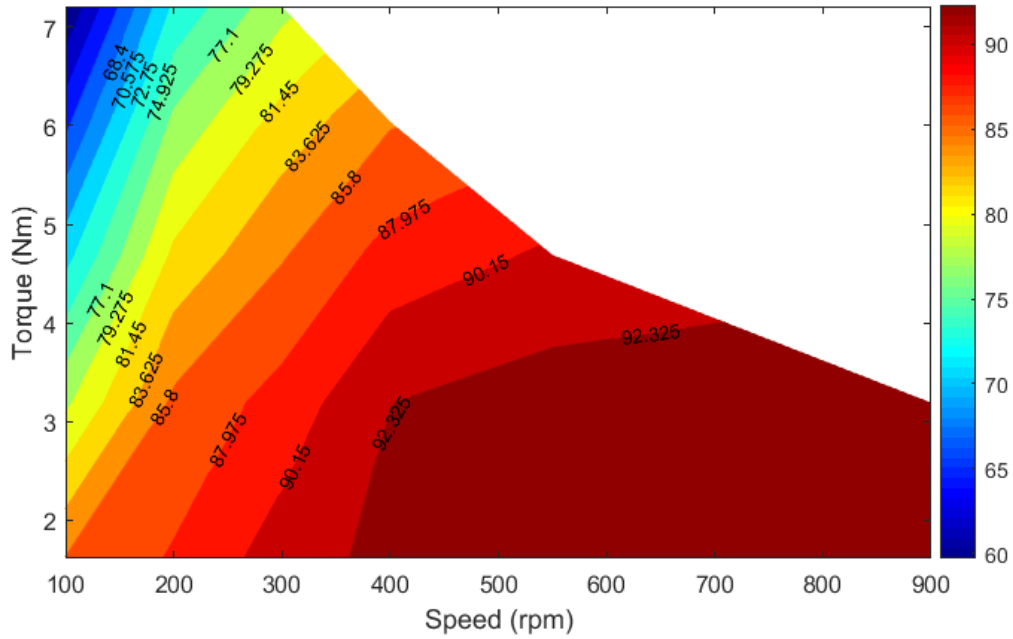


Figure 4.9. Stator-PM TFM efficiency map.

4.3 Benchmark Comparison

Two representative TFM designs are selected from the literature as benchmark machines for comparison with the Stator-PM TFM. Table 4.2 lists the major design parameters and performance specifications.

The Stator-PM TFM is redesigned using NdFeB to show the Stator-PM TFM potential in using rare-earth magnets for high performance applications. Shown in the first two columns of Table 4.2, the two versions of Stator-PM TFM share the same outer dimensions and operating conditions with the only difference being the magnet material and geometric optimization.

Table 4.2. Benchmark Comparison for Stator-PM TFM.

Parameters	Ferrite Stator-PM TFM	NdFeB Stator-PM TFM	Ferrite TFM [34]	NdFeB TFM [9]
OD (mm)	154	154	225	160
Axial length (mm)	150	150	102	50
Air gap (mm)	1	1	1	0.4
Pole number	24	24	30	50
Frequency (Hz)	60	60	100	119
PM material	Ferrite C12	NdFeB N35SH	Ferrite	NdFeB 35
Iron material	Somaloy Prototype	Somaloy Prototype	M19 steel	Somaloy 3P
Current density (A/mm ²)	5	5	5	6.6
Speed (rpm)	300	300	400	285
Power (W)	678	1338	1200	240
Torque (Nm)	21.6	42.6	28.6	8.14
Torque density (Nm/L)	7.75	15.3	7.06	8.14
Torque density (Nm/kg)	1.84	3.47	3.28	2.01
Efficiency	78.6%	87.6%	N/A	N/A
Power factor	0.33	0.73	0.202	N/A

The benchmark Ferrite TFM in [34] has double-sided stator and flux-concentrated rotor with two axial air gaps in one phase. This is the same TFM topology as that introduced in Chapter 1.

The NdFeB TFM in [9] has a flux-concentrated outer rotor with rare-earth magnets, and an SMC stator utilizing mutual flux path. Compared to both the benchmark machines, the designed ferrite Stator-PM TFM has roughly comparable performances in terms of torque density, even though one of the benchmark TFM relies on magnets that are more powerful. The efficiencies of the two benchmark TFMs are not available to compare with that of Stator-PM TFM.

The Stator-PM TFM using NdFeB exhibit definite advantages over the benchmark machines. This can be considered as the high-performance version of Stator-PM TFM that shares the same construction simplicity as the ferrite Stator-PM TFM, but uses much less magnet volume while exhibiting much higher torque density, efficiency, and a power factor that's comparable to regular PMSMs.

4.4 Conclusions

This chapter builds upon the knowledge gained through studies in the first three chapters, and designed the best possible ferrite-magnet-based TFM for direct-drive traction application. 3D FEA analysis demonstrates that the Stator-PM TFM topology excels in terms of resistance to PM demagnetization, low cogging torque, extended constant power speed range, and high efficiency. Benchmark comparison shows the designed TFM exhibits balanced performance in terms of torque density, efficiency and power factor.

CHAPTER 5 MULTI-PHYSICS DESIGN AND PROTOTYPE CONSTRUCTION

This chapter describes the process of successfully building a one horsepower Stator-PM TFM prototype, which will be used in experimental tests to verify the electromagnetic design and performance.

First step in the prototyping process is the multi-physics design, calculation and simulation of the machine, particularly on the structural and thermal aspects. The proposed Stator-PM TFM topology has drastically different structure compared to not just conventional radial flux machines, but also to any other transverse flux machines. The unique structure, as well as the use of novel core material, necessitates detailed calculation and simulation on mechanical stress and deformation, to ensure safe operation of the prototype during experimental testing.

Secondly, thermal design for a traction motor is equally as important as electromagnetic design, because the continuous and peak torque output of the motor are ultimately limited by thermal constraints. Excessively elevated temperature also leads to lowered efficiency and premature aging of winding insulation. This chapter describes the assumptions made in 3D FEA thermal simulation, and the details considered during the prototype construction to facilitate heat dissipation.

Finally, having learnt from the multi-physics simulation results, a one horsepower TFM prototype is fabricated in-house. The second part of this chapter describes in detail the prototype fabrication procedures, the considerations and compromises made, as well as the lessons learned toward future prototyping efforts.

5.1 Structural Analysis

Stator structure of the stator-PM TFM is inherently robust, thanks to its self-locking mechanism. The wedge-shaped SMC and ferrite pieces are supported by the rigid copper ring

winding on the inside, and are supported by the aluminum frame on the outside. Once the stator poles are assembled around the winding and then shrink-fitted into the motor frame, the compressive force will tightly push all the pieces against each other, as well as against the copper ring. The only uncertainty regarding stator structure is that how much interference is allowed, before the mechanical stress exceeds the compressive yield strength of the brittle SMC and ferrite materials. If the interference between the stator assembly and the frame is too small, the shrink fit cannot achieve desired strength; if the interference value is too large, the mechanical stress caused by shrink fit may crush the stator material.

An online interference fit calculation tool [35] is first used to give an initial estimate of the interference value. Input values include hub and shaft dimensions, as well as material mechanical properties. Output of the calculation tool gives maximum Von Mises stress on both the hub and shaft, and the safety factors against material yield strength. By varying the amount of interference and observe the stress results, an interference amount of 0.1 mm is chosen as the preferred value, which gives 27 MPa maximum stress and safety factors of at least 2.

In order to verify this optimum level of interference, static FEA structural simulation is conducted in Solidworks. In the simulation model, the stator assembly has an outer diameter of 154.1 mm, while the motor frame has an inner diameter of 154 mm. The material properties for each part are listed in Table 5.1 below, and act as parameters for the simulation model. Other boundary conditions include fixed support at the contact surfaces between the frame and the end plates, motor stays at room temperature, and no external forces acting on any part. The simulated steady state Von Mises stress is plotted in Figure 5.1(a)(b). Close examination of Figure 5.1(b) reveals that the maximum stress value is below 90 MPa, and is located along the edge of the contact surface.

Table 5.1. Material Mechanical Properties.

Material property	Aluminum	SMC	Ferrite
Tensile strength (MPa)	310	15	34
Compressive strength (MPa)	N/A	140	895
Modulus (MPa)	69e3	10e3	18e3

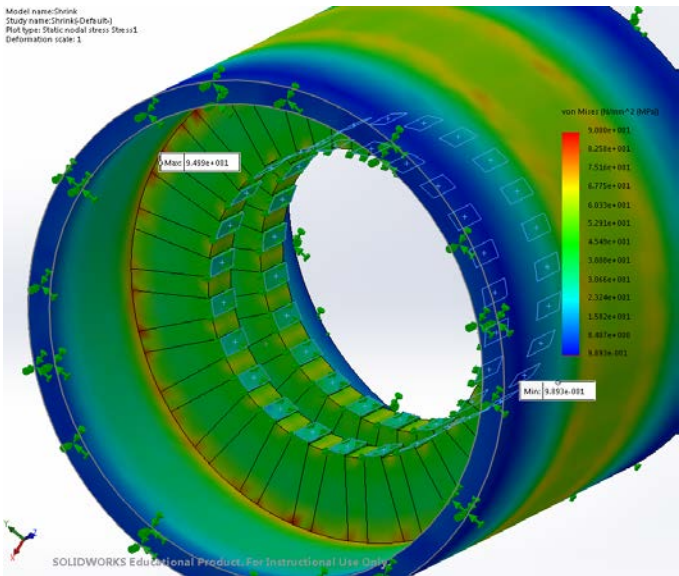


Figure 5.1. (a) Structural simulation Von Mises stress.

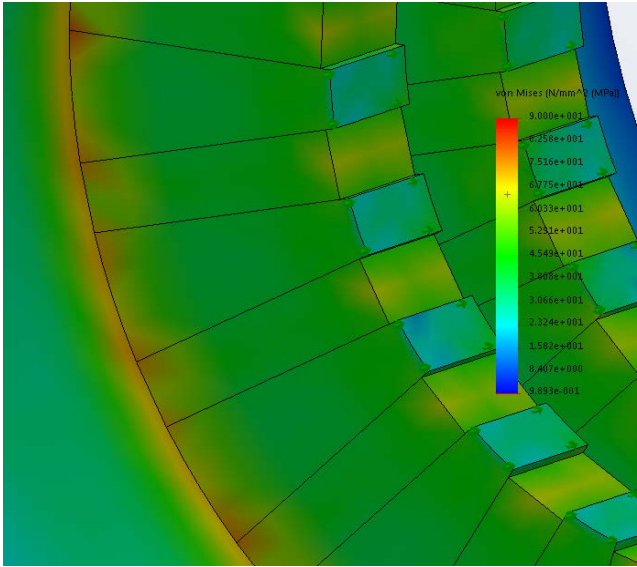


Figure 5.1. (b) Structural simulation Von Mises stress.

To further reduce the stress on the stator assembly, one design technique is used, in which rounded fillets are introduced on the edges of SMC core and ferrite magnets, as illustrated in Figure 5.2(a). By incorporating the fillets, the maximum stress along the edge of the contact surface is effectively reduced, as shown in the simulation results in Figure 5.2(b)(c). The final resultant stress level of less than 60 MPa is well within the mechanical limits of both SMC and ferrite.

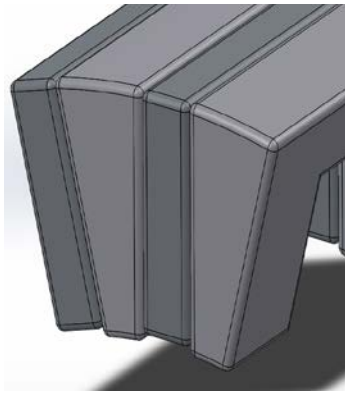


Figure 5.2. (a) Rounded fillet.

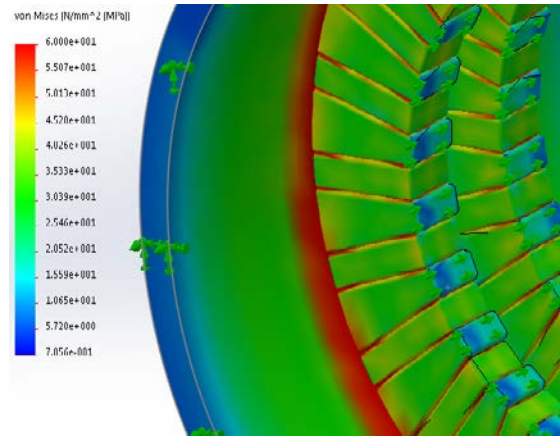


Figure 5.2. (b) Von Mises stress with fillet.

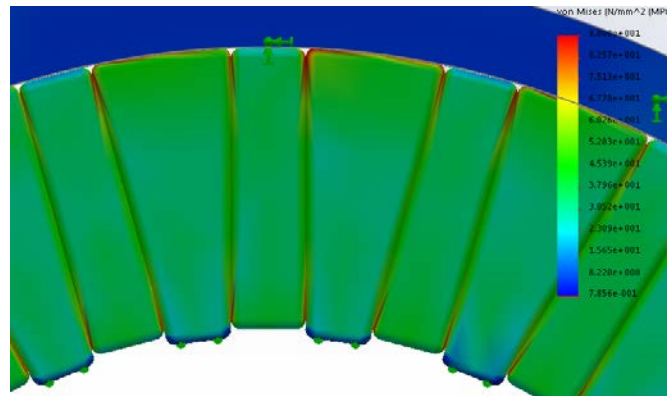


Figure 5.2. (c) Von Mises stress with fillet.

5.2 Thermal Analysis

Thermal design is equally as important as electromagnetic design in ensuring a machine's optimal performance. For a certain loss distribution in a machine, good thermal design translates to lower continuous operating temperature, which in turn leads to less copper loss and higher

efficiency, and statistically ensures longer service life of the insulation system and the bearings [36].

In order to estimate the steady state thermal behavior of the TFM, and to provide design guidelines for heat conduction path, a FEA based thermal analysis is performed before construction of the TFM prototype. The 3D Stator-PM TFM model, shown in Figure 5.3, is constructed in Solidworks software, with relevant details and boundary conditions that pertains to steady state thermal calculation. Heat sources for the thermal simulation includes 45W copper loss in the stator windings, as well as 10W and 5W core loss in stator and rotor, respectively. Table 5.2 lists thermal conductivity parameters for various materials used in the machine.

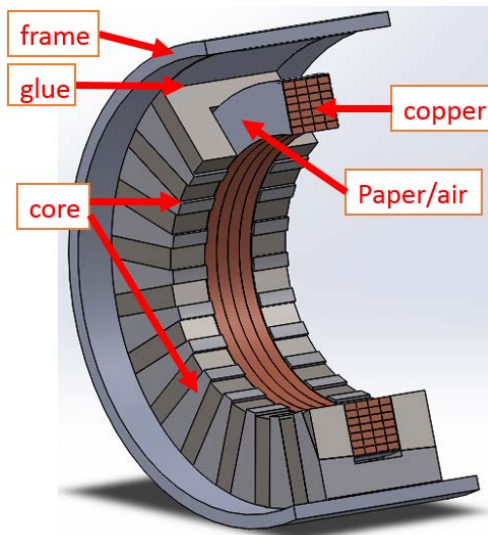


Table 5.2. Material Thermal Conductivity Parameter.

Material	Thermal conductivity (W/m·K)
Copper	390
Somaloy	47
Ferrite	29
Aluminum	209
Insulation paper	0.22
Glue	0.22
Air	0.024

Figure 5.3. TFM model for thermal simulation.

The challenge in conducting an accurate thermal simulation lies in determining the proper boundary conditions that reflect the actual physical reality of the prototype machine. Most boundary conditions, such as the loss distribution, can be determined with reasonable confidence in accuracy. However, considerable uncertainties exist in the following three boundary conditions.

- The contact surface between copper winding and stator cores: this interface consists of a thin layer of insulation paper, with $0.22 \text{ W/m}\cdot\text{k}$ thermal conductivity and 0.25 mm thickness, and much less thermally conductive air pockets whose thicknesses are unevenly distributed.
- The contact surface between stator cores and frame: similar to the above condition, with an unknown mixture of air and glue. The air trapped in the contact surface, because of its low thermal conductivity, will constitute the vast majority of resistance in the thermal path. Figure 5.4(a) and (b) below compare the case where the contacts are perfect and the case where the entire contacts are air gap. The maximum temperature point, which is in the stator winding, ranges from 80°C for the best scenario to 142°C for the worst. The physical reality, as well as the resulting temperature, will fall in between these two extreme scenarios.

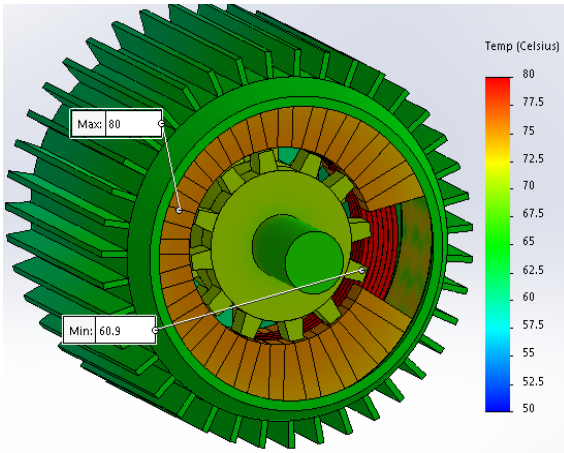


Figure 5.4. (a) Perfect contact scenario.

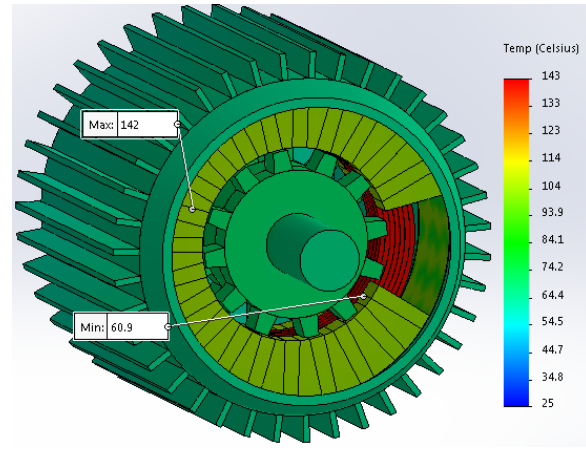


Figure 5.4. (b) Worst contact scenario.

- The convective interface between frame and atmosphere: the convective coefficient on the frame surface depends on the speed of airflow. Two distinct cases are studied and presented in Figure 5.5(a)(b), where the current density is ramped up to 8 A/mm^2 . In the Totally Enclosed Non-Ventilated (TENV) scenario in Figure 5.5(a), in which no forced air movement is present, the convection coefficient is estimated at $5 \text{ W/m}^2\cdot\text{K}$ [36]. In a Totally Enclosed Fan-Cooled

(TEFC) scenario in Figure 5.5(b), in which a tail fan forces the air to flow through the frame fins, the airflow speed depends on the operating speed of the motor. At 300 rpm rated speed, the air speed between the fins are assumed 1 m/s, which translates to $20 \text{ W/m}^2\cdot\text{K}$ convection coefficient [36].

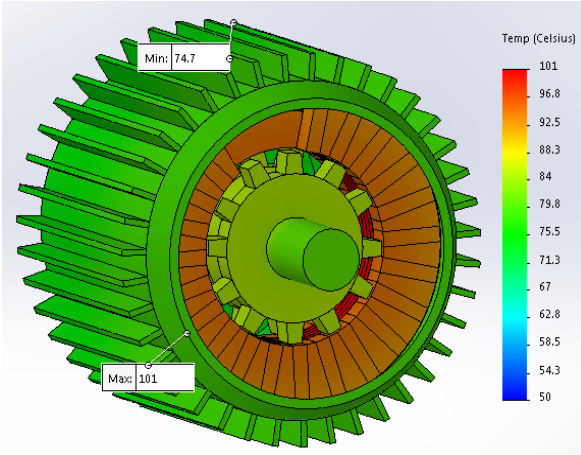


Figure 5.5. (a) TENV with $5 \text{ W/m}^2\cdot\text{K}$.

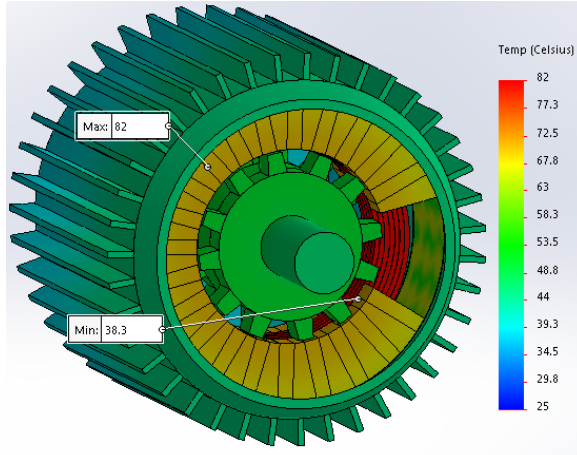


Figure 5.5. (b) TEFC with $20 \text{ W/m}^2\cdot\text{K}$.

However, the coefficients assumed in this simulation are rough estimates, acquiring the exact numbers requires Computational Fluid Dynamics modeling, which is beyond the scope of this research. As a more practical approach, experimental temperature measurement will provide vital information to fine tune the thermal simulation model. With temperature recorded through the embedded thermocouples in various locations of the prototype motor, key thermal model parameters will be varied to match temperature mapping to that from experiment. Knowledge gained in the study will help guide future thermal path designs.

5.3 Prototype Machine Construction

In order to establish the validity of 3D FEA simulation results and analysis, the author has constructed a prototype Stator-PM TFM. Thanks to Stator-PM TFM's unique topology, its

construction sequence is completely different from that of a conventional permanent magnet or induction machine. In conventional machines, the stator construction typically starts with press fitting the stacked laminations into the frame, then proceeds to place insulation material in the numerous winding slots, after which small coil groups are inserted into the slots, and finally makes terminal connections among the poles and phases to finish the winding configuration. Whereas in the studied TFM, whose stator model is shown in Figure 5.6, the prototype construction starts with the concentrated copper winding. Once the ring winding is finished and insulated, stator pole pieces and permanent magnets are assembled around the winding, which also acts as a structural support. The complete stator assembly would then be fitted into the motor frame. Despite the rather unconventional building method, the prototype strives to incorporate design features that facilitate mass production. Those features include standard motor frame, the easily automated ring-shaped winding, and the simplicity of a magnet-free rotor.

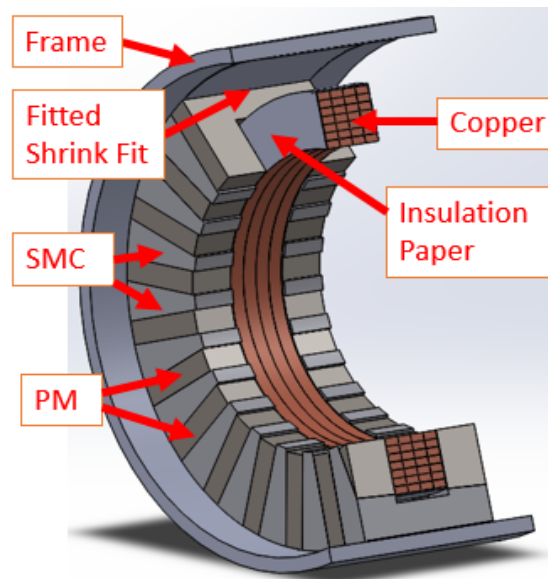


Figure 5.6. TFM prototype stator structure design.

5.3.1 Winding

Constructing the ring winding is the first step in the prototype fabrication process. Because the winding also acts as a structural support for later stator assembly, its finished dimensions need to be precise. The proposed TFM has designed for the slot dimension to be 20 mm by 20 mm square, such that a simple winding bobbin, as shown in Figure 5.7(a), could be used to assist the winding process and help regulate the dimensions. The 3D-printed plastic bobbin has three individual parts that are joint by four screws, so that we can easily remove and reuse the bobbin after finishing the winding. Four more openings are also incorporated in the sidewalls of the bobbin, through which zip ties can temporarily hold the copper wires in place during the construction process.

There are two options in selecting the wire gauge. One option is to use the thin stranded round wire that is commonly used in such small machines. Thin wires are flexible and easy to wound, and offer reasonably high fill factor thanks to the simple winding shape. For example, AWG22 magnet wire is used to build the coil shown in Figure 5.7(b), in which 65% fill factor is achieved. However, this wire option is only suitable for high voltage low current machines, since there are many serial turns.

The other option, which the final prototype chooses, is to use thick rectangular wire. The uniform slot area, combined with the simple shape of the ring winding, enable the use of form-wound, bar-type rectangular wire to achieve even higher fill factor. Figure 5.7(c) is the 2.31 mm×4.62 mm cross-section rectangular magnet wire, which is AWG7 equivalent with 10.5 mm^2 copper area. With the assistance of the winding bobbin, 30 turns of wire is wound into the finished winding in Figure 5.7(d)(e). Adhesive and zip ties help in securing the copper wire in place for an extended period of time until the spring force is released. By arranging large gauge rectangular

wire into a tightly wound ring winding, the stator-PM TFM has achieved 75% slot fill factor with hand tension. Even higher fill factor is achievable with high winding tension from a winding machine. The TFM's winding manufacturing can be easily automated in mass manufacturing thanks to its simple winding shape.

Finally, to ensure good electrical insulation and good thermal conduction, two layers of insulation material are applied to the outer surface of the ring winding. The first layer is Kapton tape coated with a thin layer of silicone, of which the Kapton acts as electrical insulation, while the soft silicone fills the gap between the winding and stator cores, thus providing better thermal conductivity. The second layer is insulation paper, which, other than electrical insulation property, also offers abrasion resistance in case there are movement between the winding and stator cores. The finished winding is shown in Figure 5.7(f).

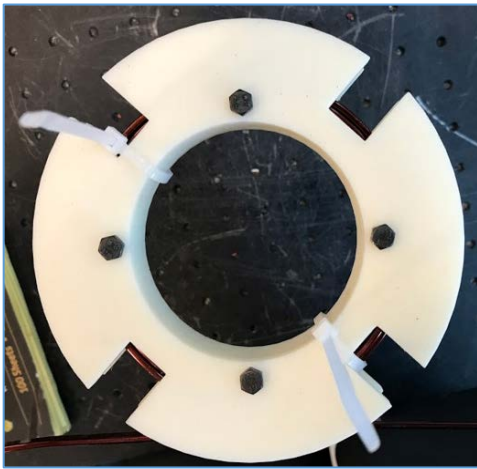


Figure 5.7. (a) Winding bobbin.



Figure 5.7. (b) Ring winding with thin wire.



Figure 5.7. (c) Rectangular wire.

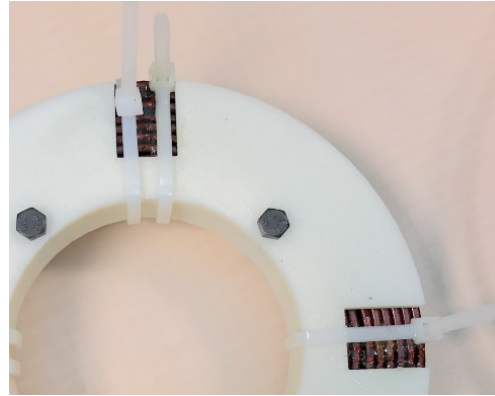


Figure 5.7. (d) Winding within bobbin.



Figure 5.7. (e) Finished winding.

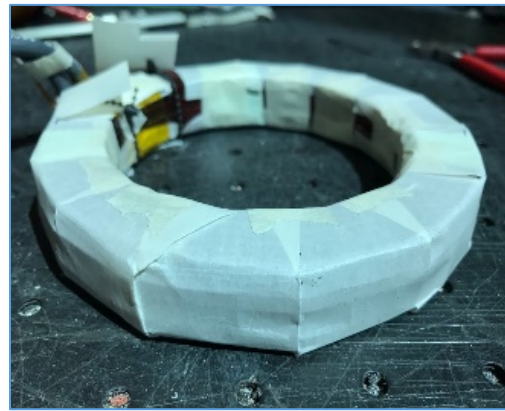


Figure 5.7. (f) Winding with insulation.

5.3.2 Stator

The stator core uses Soft Magnetic Composite (SMC) material to provide three dimensional flux path. The SMC is made of iron powder particles that are surface insulated, and pressed to the desired shape in one single compaction step. This low cost powder metallurgy method saves both raw material and processing procedures. However, in the prototyping scenario, neither compaction equipment nor tooling is available. For building a prototype, the material supplier offers a pre-fabricated cylindrical blank, called Somaloy Prototyping Material (SPM) [37], as shown in Figure 5.8(a). The SPM has enhanced machinability, and through conventional machining techniques,

such as turning, drilling and milling, can be machined into the desired stator core shape, as shown in Figure 5.8(b).

The ferrite magnets preferably should have shape that coincides with the shape of the SMC core, and magnetized in the circumferential direction. Nonetheless, to reduce the prototype cost, two shapes of common block-shaped magnets are ordered instead. As shown in Figure 5.8(c), the C-shaped magnet is replaced with separate pieces. These pre-magnetized, block-shaped ferrite magnets are then attached to the stator cores to form one pole pair. Figure 5.8(d) shows the iron core, the ferrite magnet, and assembly of one pole pair.

In total, 24 poles are arranged around the winding to create the single-phase stator assembly, shown in Figure 5.8(e). The aluminum fixture has the same diameter as the motor frame. It is used only in the assembling process, and is removed once the stator assembly is finished. The stator cores and magnets are in close contact with the sidewalls of the winding to facilitate heat dissipation from the winding to the motor frame. Thermal couplers have been placed at various parts of the stator winding for real time temperature measurement.



Figure 5.8. (a) Somaloy Prototyping
Material blank.



Figure 5.8. (b) Stator core.



Figure 5.8. (c) Ferrite magnet blocks.



Figure 5.8. (d) One pole pair assembly.

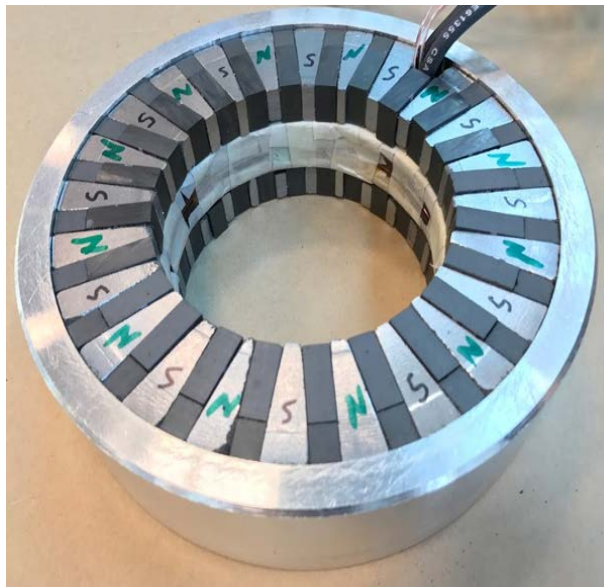


Figure 5.8. (e) Finished stator with aluminum fixture.

5.3.3 Rotor

Figure 5.9(a)(b) shows the rotor parts and the finished rotor, respectively. There are three individual pieces, two of which are sidepieces with twelve teeth each, and one rounded centerpiece. Precision drilled pinholes guarantee the proper phase shift between the two sets of teeth by inserting a pin. Similar to the stator, the rotor iron cores are machined to the desired shape from the cylindrical SMC blank, then bonded together with adhesives. In mass production scenario,

both the stator and rotor cores will come directly from mold compaction, with minimal material waste.



Figure 5.9. (a) Rotor Parts.

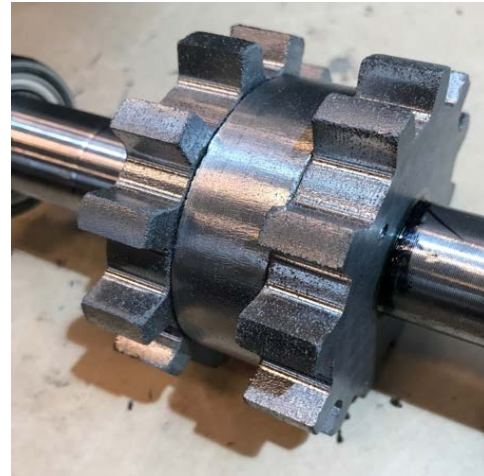


Figure 5.9. (b) Finished Rotor.

5.3.4 Housing

Figure 5.10(a)(b) is the stator and rotor being fitted into a standard NEMA 143T aluminum frame. Because of relatively poor machining precision in the lab environment, in order to stay on the safe side and avoid touching between rotor and stator, a larger than usual 1.5mm physical airgap is maintained between the stator and rotor. The motor housing is from a commercially available 1-hp induction machine, whose original laminations are pulled out and replaced with the TFM stator and rotor. By reusing the frame, end plates, bearings and shaft, considerable time, cost and engineering effort are saved. Moreover, the standard frame with 3.5 inch shaft height is compatible with existing dyno testing setup in the lab, thus greatly simplified the test motor mounting process. The finished prototype is in Figure 5.10(b). By basing the stator-PM TFM's mechanical structure on an outer stator inner rotor radial flux machine frame, thereby combining

the ring winding's simplicity and the conventional structure's proven reliability, the manufacturing of TFM is significantly simplified.



Figure 5.10. (a) Stator and Rotor Fitted Inside Frame.



Figure 5.10. (b) Finished TFM Prototype.

5.4 Discrepancies between Initial Design and Finished Prototype

Due to limitations in part availability and mechanical tolerance, the finished prototype deviates from the initial in several aspects. Below, we summarize the implications of those deviations, and whether more efforts could have been made in the design and prototyping process to avoid the discrepancy. This consideration will serve as a valuable experience for future attempts to build prototypes of TFM or other novel motors.

- **Housing size:** The stator outer diameter of 154mm for the original design was based on the bore dimension provided in the product drawing of the motor housing. However, the measured inner diameter of the prototype frame is only 152mm. This difference, though relatively small, still means proportionally shrinking the air gap diameter, which has a squared relationship with output torque.

- Magnet thickness: the ferrite magnets were ordered according to initially envisioned frame size, which would have offered 164mm as stator outer diameter. The magnet's thickness at 7.45mm would translate to core-span-factor $K_s=0.55$, which is the optimized value for optimal electromagnetic performance. Unfortunately, the eventually used motor frame only provides 152mm available diameter. As a result, the prototype has $K_s=0.38$, which reduces the stator teeth area by 31%. With the reduced teeth area, at low current levels, the same amount of flux will still flow through the area with increased flux density. However, at higher current levels, the smaller flux path would cause the stator teeth to saturate earlier, thus limiting the peak torque performance.
- Air gap length: The electromagnetic design assumed 1mm as the air gap length. This value, even though already big for production motors of this size, is a typical number used for a lab-built prototype. Despite the conservative selection of air gap length, the poor machining tolerance during prototype construction further erodes the author's confidence in guaranteeing enough clearance between the stator and rotor. Eventually, decision was made to machine the rotor outer diameter to be 3mm less than the stator inner diameter, thus trading electromagnetic performance in exchange for successful rotation of the prototype. This discrepancy turns out to be the major sacrifice, as it reduces the no load back-EMF by 30% compared to the case using 1mm air gap. The no-load back-EMF at 300rpm is simulated at various air gap lengths, with the rms values plotted in Figure 5.11. It shows even 0.25 mm decrement in air gap length offers considerable boost in back-EMF. Looking back, given the abundance of time and resources, the author should have taken more risk in making the air gap smaller in the first try. Should the first rotor fail, a second or more rotors could then be made with incrementally increasing air gap.

The effect from an increased air gap length is even more pronounced in this design because a high flux concentration factor is used in the stator-PM topology. Equation (1) is a simplified magnet flux density derivation assuming the ferrite's relative permeability is 1:

$$B_{PM} = \frac{L_{PM}}{L_{PM} + K_f \cdot L_{gap}} Br \quad (1)$$

In this equation, L_{PM} is the magnet's thickness, K_f is the flux concentration factor, L_{gap} is the air gap length, and Br is residual flux density of the magnet. Because this design uses a high flux concentration factor of 7 in its stator magnetic circuit in order to boost the air gap flux density, the consequence of increasing the air gap length from 1 mm to 1.5 mm is magnified, as seen in the two equations below:

$$B_{PM} = \frac{7.5 \text{ mm}}{7.5 \text{ mm} + 7 \cdot 1 \text{ mm}} \cdot 0.4 = 0.21 \quad (2)$$

$$B_{PM} = \frac{7.5 \text{ mm}}{7.5 \text{ mm} + 7 \cdot 1.5 \text{ mm}} \cdot 0.4 = 0.17 \quad (3)$$

This drop in PM's operating flux density leads to the proportional decrease in air gap flux density, which eventually causes the reduction in back-EMF magnitude and torque capability of this prototype.

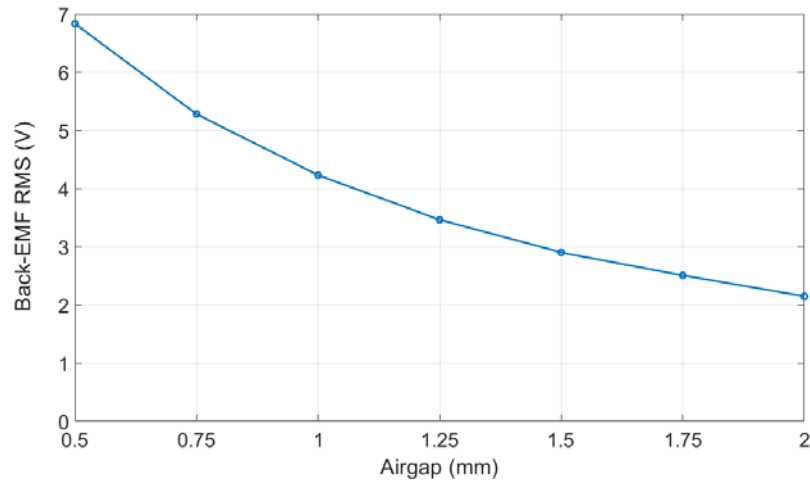


Figure 5.11. Back-EMF rms value as a function of airgap length.

- PM material property: during the design stage, the FEA model used the PM material property, namely intrinsic coercivity of 318 kA/m and residual flux density of 0.4 Tesla, as provided by the magnet supplier. Later, the ferrite magnet samples used for building the prototype were measured using a Fluxmeter and Helmholtz coil. The measured B-H curve of the sample magnets is plotted in Figure 5.12, together with the datasheet B-H curve.

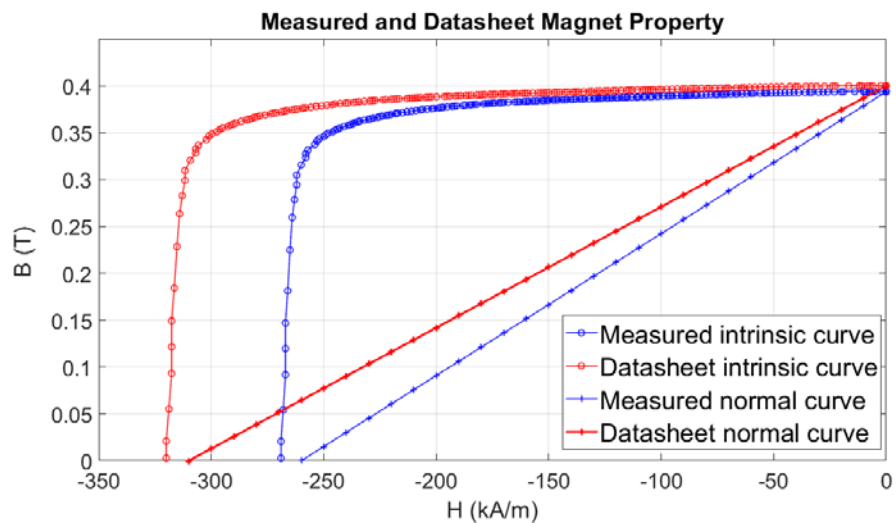


Figure 5.12. Measured and datasheet permanent magnet property.

The result reveals that even though the residual flux density roughly matches with the material description, the intrinsic coercivity and coercivity is only 269 kA/m and 259 kA/m, respectively. Reduction in coercivity will lower the magnet's permeance coefficient in the magnetic circuit, which in turn lowers the operating flux density of the magnet. Furthermore, the situation is exacerbated by the stator-PM TFM's unique magnetic design, which utilizes a rather high flux concentration factor that relies on coercivity to maintain air gap flux density. Moreover, the reduced intrinsic coercivity will pose more risk of demagnetization, especially at lower temperatures.

These discrepancies necessitates the original FEA simulation model to be updated with new geometric dimensions and material properties to better reflect the real prototype motor. In the next chapter, the results from the updated FEA model will then be compared with the experimental results of the prototype, for the purpose of validating the simulation model.

5.5 Conclusions

The structural and thermal FEA simulations have offered useful guidelines in the construction of TFM prototype. Efforts are made to enhance the motor's structural reliability, as well as to improve the thermal path for effective cooling. A newly invented motor construction sequence better accommodated the unique structure of stator-PM TFM. The in-house-built prototype demonstrated the feasibility of fitting TFM into standard motor housing. The modular structure, concentrated winding, and inner solid rotor configuration all contribute to easier automation and lower cost for mass production. Thorough analysis of the discrepancies between the design and the actual prototype reveals the practical limitations in the lab fabrication process, and provides valuable lessons for future prototyping attempts.

CHAPTER 6 EXPERIMENTAL SETUP AND TEST RESULTS

This chapter details the experimental setup for testing the TFM prototype, and the various tests performed to evaluate the electromagnetic and thermal performance. Test results provide both instantaneous waveforms and averaged steady state measurements. The experimental results are then compared with those from FEA simulation to offer more insight, and to provide valuable feedback information in retuning the simulation model.

6.1 Experimental Setup

The prototype TFM is mounted on the dynamometer testbed for experimental evaluation of its no-load, loaded, and thermal performances. The entire setup, including measurement and data acquisition equipment are shown in Figure 6.1. The TFM is coupled to a 10 horsepower induction machine, which acts as the load motor. In between the two motors, a Himmelstein torque transducer, rated at 500 lb-in, measures torque and speed. Under no-load condition, the load motor is driven by an ABB ACS-800 four quadrant drive to maintain constant speed, while the TFM's terminal is open circuit. Under loaded condition, the load motor acts as a generator with constant speed control, while the TFM acts as a motor supplied with constant dc current provided by a Magna-Power Electronics power source. Data acquisitions include Yokogawa WT3000 power analyzer for input power measurement, Agilent 34972A data logger for temperature recording, and Himmelstein data conditioning unit for filtering and logging torque and speed measurements. The oscilloscope is used in the control code debugging process, as well as measuring TFM's voltage and current waveforms for harmonic analysis.

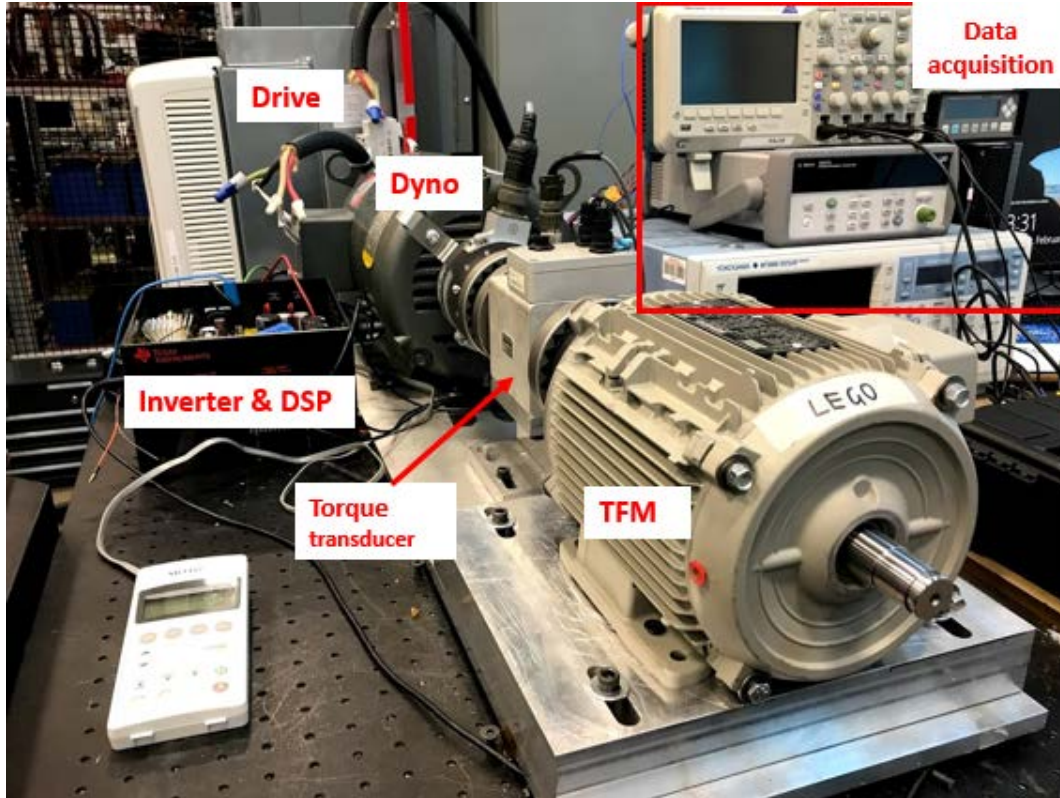


Figure 6.1. Experimental setup.

6.2 No-load Tests

No-load tests provide machine performance in terms of back-emf constant, cogging torque and friction and windage loss. In the no-load test, the TFM has its terminals open, while the dyno motor drives the TFM at various constant speeds.

6.2.1 Back-EMF

The TFM is run from 100 rpm to 600 rpm with 100-rpm increment, with the open circuit voltage measured by the power analyzer and observed in the oscilloscope. The back-EMF rms values are plotted in Figure 6.2(a) with respect to speed up to 600 rpm. As expected, the back-EMF magnitude is proportional to speed. From Figure 6.2(a), the experimental back-EMF constant is 0.0102 V/rpm, which closely matches with 0.0097 V/rpm obtained from the updated FEA model. Figure 6.2(b) shows several electrical cycles of back-EMF waveform at 600 rpm. Figure

6.2(c) is the Fourier series of the waveform. Here we choose to show the result at 600 rpm, because the speed regulation is better at this higher speed, and that harmonic content of the waveform does not change with speed. It shows the designed TFM has minimal harmonics in its waveform, which means when supplied with sinusoidal phase current, there will be low torque ripple resulting from harmonic interaction between flux linkage and current.

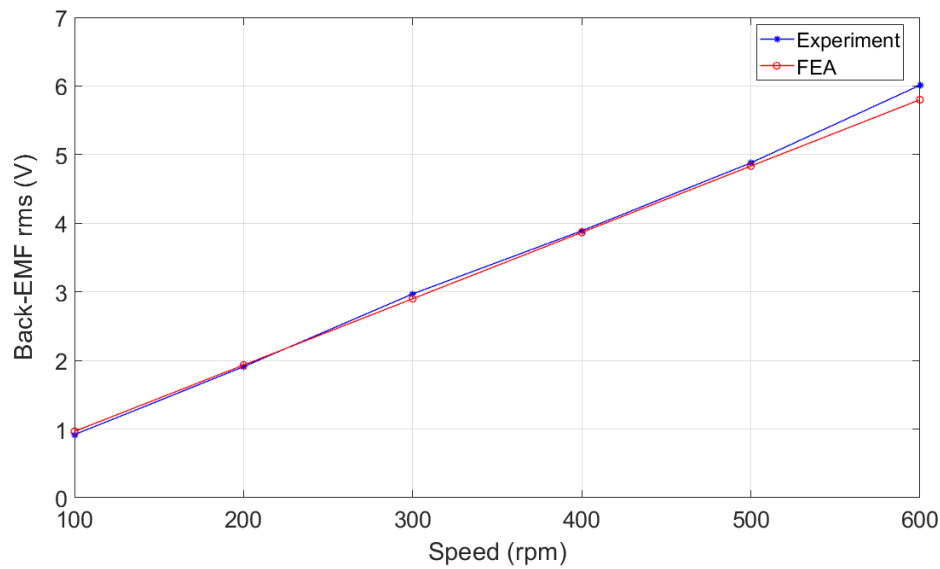


Figure 6.2. (a) Back-EMF rms value with respect to speed.

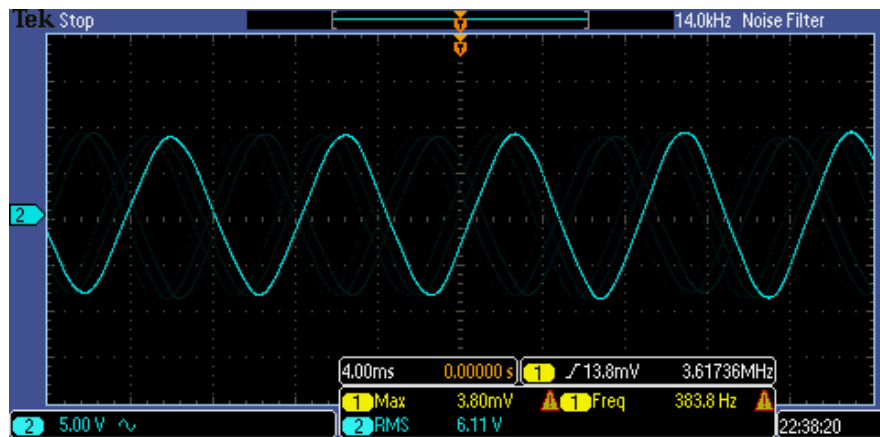


Figure 6.2. (b) Experimental back-EMF waveform at 600 rpm.

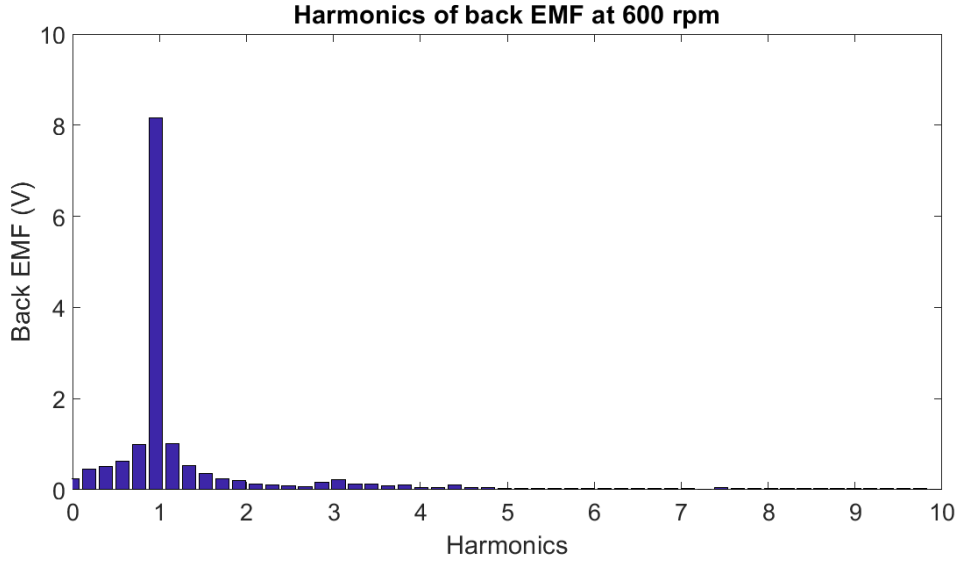


Figure 6.2. (c) Experimental back-EMF harmonic spectrum.

6.2.2 Cogging torque

In the electromagnetic design and simulation of the TFM, extra attention was given to reducing the cogging torque. Part of the no load testing aims to measure the real-time cogging torque and extract its harmonic contents, as a verification of the teeth-shifting method adopted in the design. However, accurately measuring the cogging torque is always challenging, especially with the available lab equipment. In this experimental setup especially, there are several practical challenges that make accurate cogging torque measurement difficult. Several mitigation methods are taken to reduce the effect of those limitations.

- In this high torque dyno testbed, measuring range of the torque transducer is 56.5 Nm while the expected cogging torque magnitude is less than 1 Nm, which means the measured data has low resolution.
- The torque transducer has a hardware low-pass-filter with cut-off frequency at 100 Hz. Therefore, the TFM needs to operate at very low speed for cogging torque measurement, to ensure the cogging torque harmonics are well within the cut-off frequency.

- Operating at constant low speed is a stringent requirement on the dyno drive. A shaft mounted position encoder is used to supply position data to the ABB drive, so that the dyno operates with sensed vector control, thus improves the speed regulation.
- The couplings between the TFM and torque transducer, and between the torque transducer and dyno motor, have rubber parts that intend to tolerate misalignment. However, the rubber parts also create backlash, rendering cogging torque measurement inaccurate. By inserting plastic fillers into the mechanical gap within the coupling, the backlashes are totally eliminated.

With the above mentioned practical issues mitigated, the single phase prototype's cogging torque in one mechanical cycle is measured and plotted in Figure 6.3(a). The peak-to-peak single phase cogging torque magnitude is 1.6 Nm. Figure 6.3(b) is the harmonic distribution of the experimentally measured cogging torque with respect to fundamental electrical frequency, with 2nd order harmonics being dominant, as expected. The 0.1 Nm dc value in the measured torque reflects the effect of friction, windage and spin loss torque, which is discussed in the next section. Figure 6.3(c) is the close-in comparison between the experimentally measured and FEA simulated single phase cogging torque in half an electrical cycle. The two waveforms mostly match in shape and magnitude.

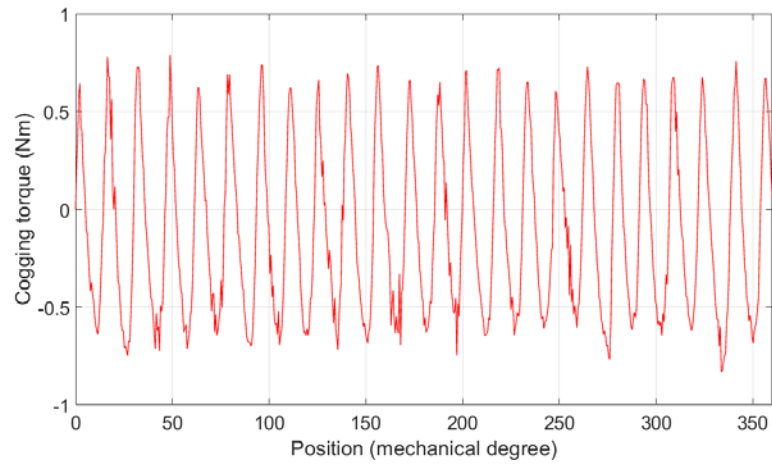


Figure 6.3. (a) Experimental cogging torque at 6 rpm for one mechanical cycle.

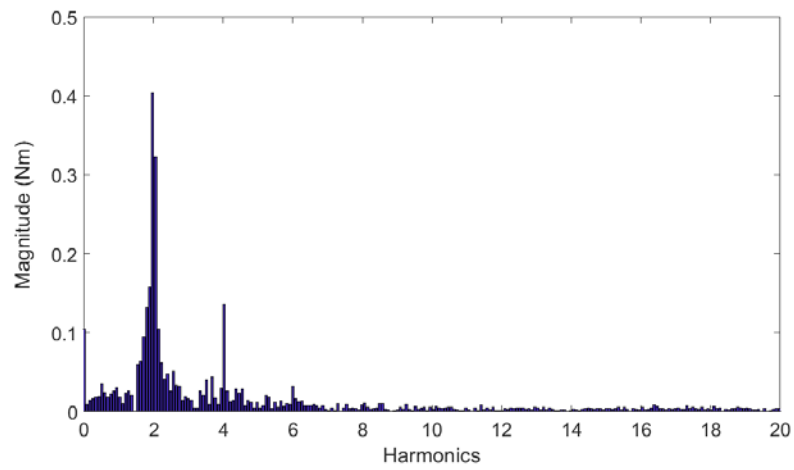


Figure 6.3. (b) Experimental cogging torque at 6 rpm harmonic distribution.

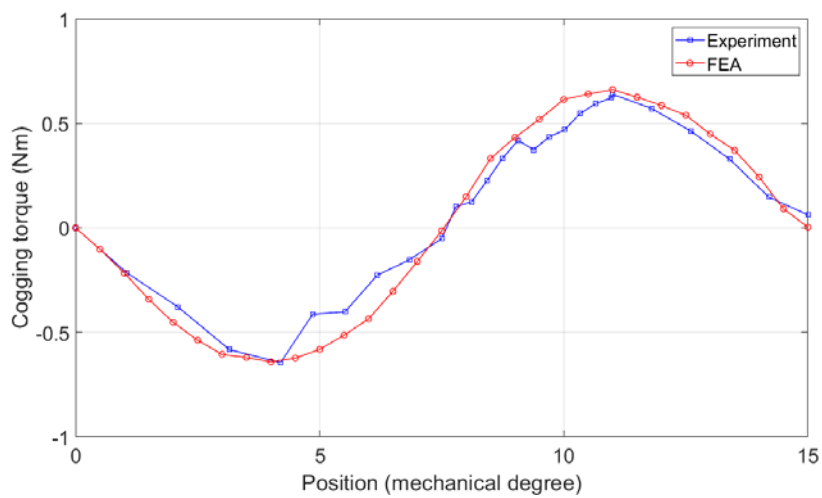


Figure 6.3. (c) Comparing experimental and FEA cogging torque at 6 rpm.

After experimentally verifying the simulated cogging torque result, the FEA simulation is then used to simulate the overall cogging torque of a three phase TFM. The simulation result in Figure 6.4(a) shows single phase and three phase cogging torques in one electrical cycle, while Figure 6.4(b) and Figure 6.4(c) shows the harmonic distribution for each of these plots. The single phase cogging torque has dominant 2nd order harmonic, which will disappear in a perfectly phase-shifted three phase machine, as is expected from the design. The three phase cogging torque only has dominant harmonics at 6th order and its multiples, but at much reduced magnitudes. The peak to peak magnitude of the three phase cogging torque is less than 0.2 Nm, which only represents 1% of the expected average torque.

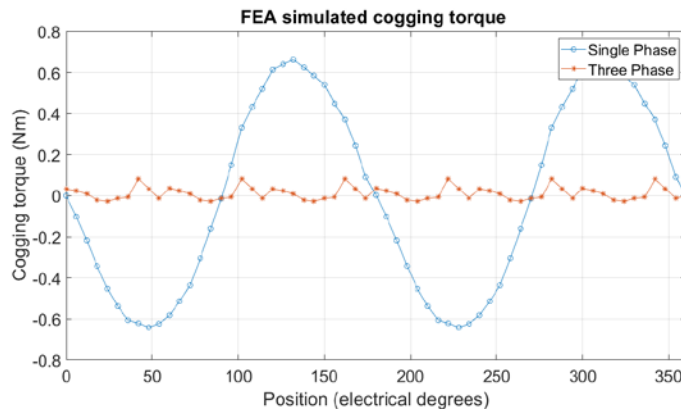


Figure 6.4. (a) FEA simulated single phase and three phase cogging torque.

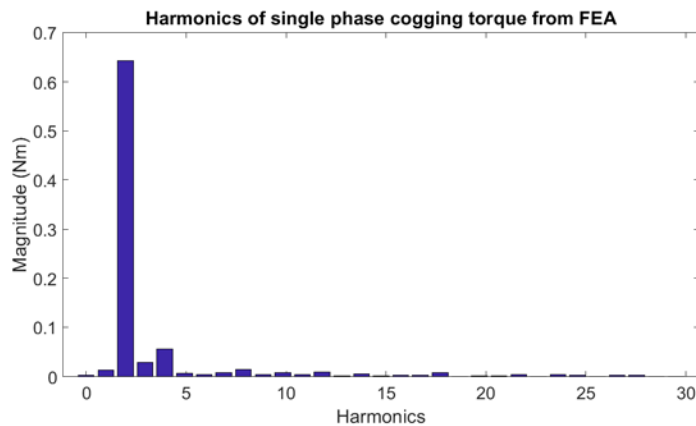


Figure 6.4. (b) Single phase cogging torque harmonics.

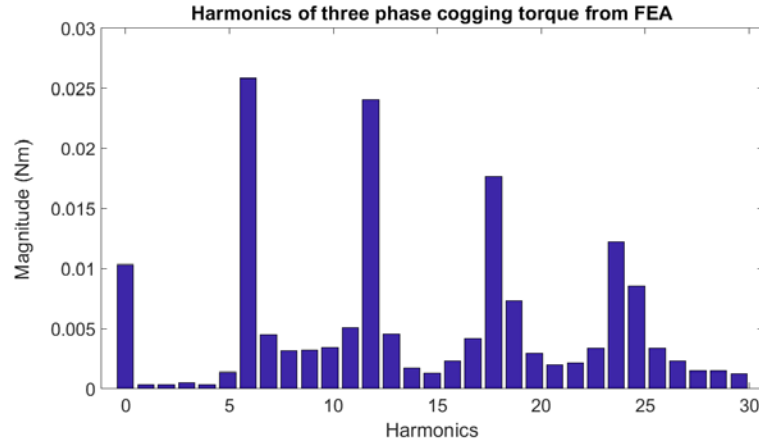


Figure 6.4. (c) Three phase cogging torque harmonics.

6.2.3 Friction and windage loss

There are two methods in obtaining the no load loss for a permanent magnet motor. One is the retardation test recommended by IEEE standard 1812, in which the motor is allowed to cruise down from a certain speed while the deceleration rate and rotor inertia are used to estimate the no load loss. The other method is to drive the open-circuited test motor with the dyno motor at various speeds, and then the measured torque represents the summation of friction, windage and no load core loss. Both methods were used to test the no load loss of a TFM prototype in [38], where it showed that the two methods give essentially the same result. Because the rotor inertia is not easily available for the retardation method, we choose to use the direct torque measurement method to obtain no load loss of this prototype.

Figure 6.5(a)(b) shows the no load torque and no load loss at various speeds. As expected, the no load loss increases with speed. The discrepancy at 400 rpm is probably caused by measurement inaccuracy because the torque value is too low for the rated range of this torque transducer. These loss data will be used in understanding the efficiency when the motor operates under load. The

friction and windage loss can also be incorporated into FEA simulation to increase its accuracy, though the separation of friction and windage loss and no load core loss is impossible, as it requires another unmagnetized rotor.

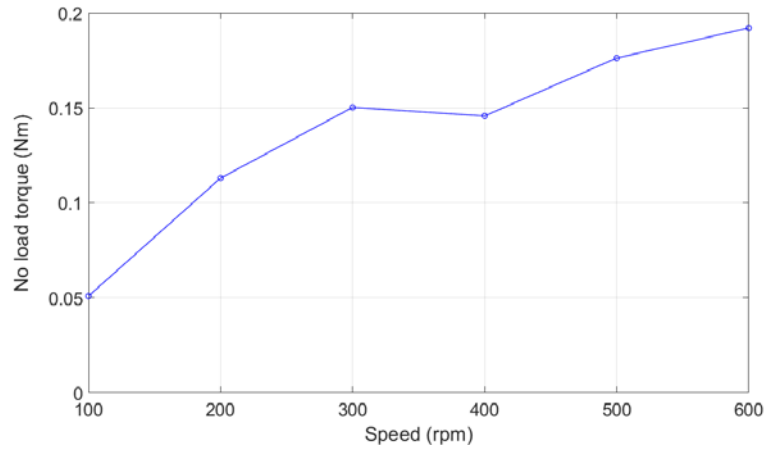


Figure 6.5. (a) No load torque at various speeds.

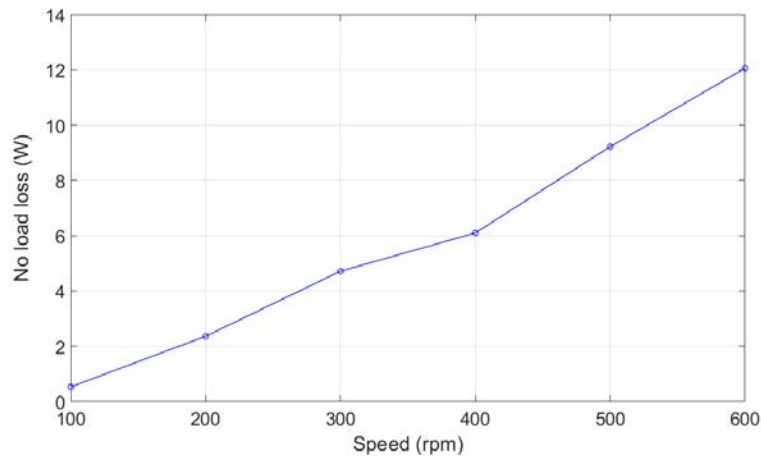


Figure 6.5. (b) No load loss at various speeds.

6.3 Torque Profile with Direct Current Excitation

For a single phase machine, a good way of verifying the load performance at various current levels is to plot its torque profile with different direct current excitations. Compared to ac excitation, which relies on rotor position information for proper vector control, dc excitation is

independent of the performance of control algorithm, thus provides a reliable way in evaluating the torque capabilities of the machine. Figure 6.6 shows the FEA simulated dc excitation torque profile for this prototype TFM. By comparing the dc torque profiles between FEA simulation and experiment, we are able to tell the validity of the simulation in predicting torque per ampere performance of the machine.

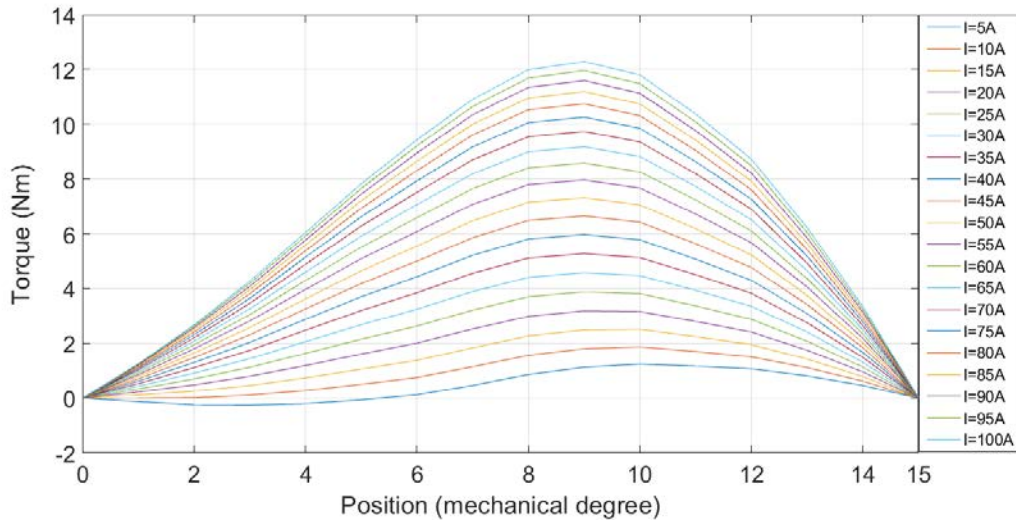


Figure 6.6. FEA simulated torque profile with direct current excitation.

The prototype TFM is supplied constant dc current with a Magna dc power supply. At each dc excitation level, the dyno rotates the TFM at a low speed while the torque profile is measured. Due to the limitation of the dyno drive's ability in maintaining constant speed under high pulsating load, only the torque profile with 5A dc current can be properly plotted and compared with that from the FEA simulation. As shown in Figure 6.7(a), the simulated torque profile closely matches with the experimentally measured torque in both wave shape and magnitude, with only less than 10% difference at peak torque. At this torque level, the dyno is able to maintain a relatively constant low speed, where the torque transducer has high enough sampling rate to provide an accurate torque profile. When the current level is further increased, the dyno motor exhibit huge

oscillation in speed, which causes distortion in the measured waveform, as shown in Figure 6.7(b), in which the distorted torque profiles are plotted with respect to dc current. Even the torque profile is distorted, the peak torque level at each current can still be captured, and be compared with the peak torques from FEA simulation. The results in Figure 6.7(c) shows for both experiment and simulation, the peak torque increases linearly with respect to current, until the saturation point.

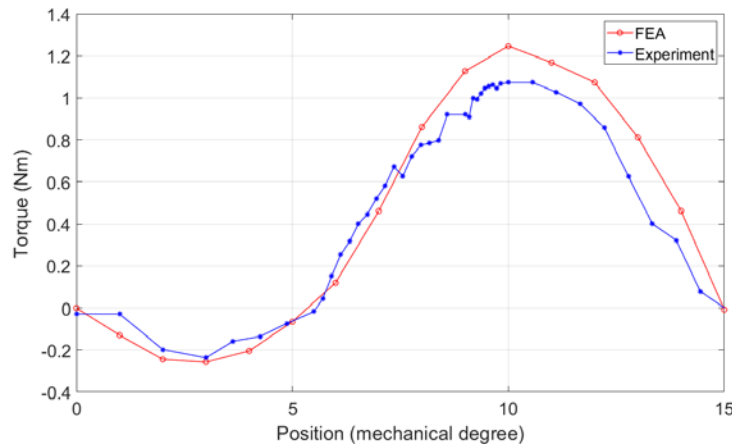


Figure 6.7. (a) Simulated and experimental torque profile with 5A dc excitation.

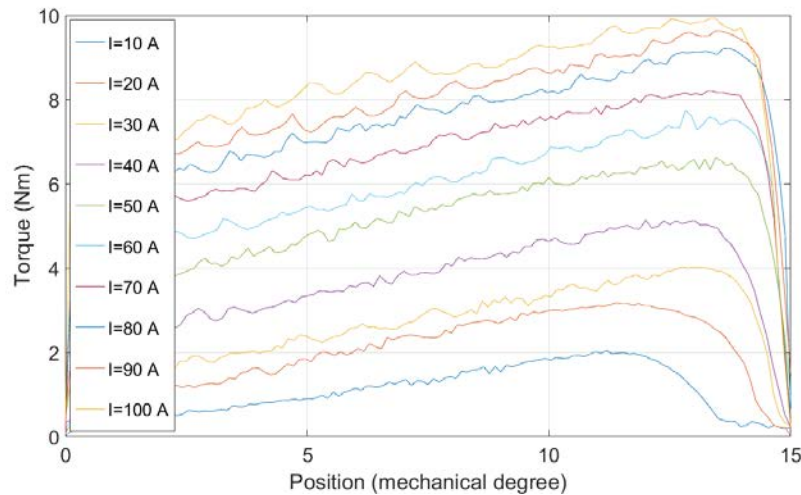


Figure 6.7. (b) Experimentally measured torque profile with dc excitation.

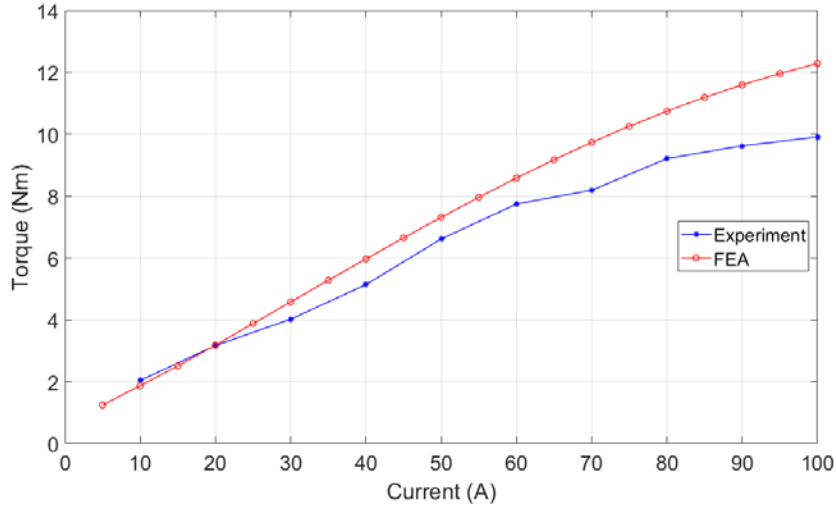


Figure 6.7. (c) Simulated and experimental peak torque with respect to dc current.

6.4 Inductance Measurement and Short Circuit Test

Inductance modeling is an important part in the design process of the stator-PM TFM, as its value relates to the field weakening, efficiency and power factor of the machine. The FEA simulated leakage inductance and the total inductance of the TFM are plotted in Figure 6.8(a), in which the highlighted data points are experimental measurements of the prototype TFM's inductances. Those measurements are taken using an Instek LCR-819 precision LCR meter. Measurement screenshots are shown in Figure 6.8(b), as the motor terminal is connected with the RLC meter, with its rotor at the aligned position due to cogging torque, while its terminal resistance and inductance values are measured when the supply frequency is 60 Hz. The measurement data are tabulated in Table 6.1. The leakage inductance is the measured inductance value when the rotor is removed. The difference in bar winding resistance and motor terminal resistance is due to the resistance of the terminal lead wires, which have extra length for ease making connections for the experiment. The simulated inductance values are in reasonable agreement with the measured ones, with the difference less than 17%.

Table 6.1. Summary of Resistance and Inductance Measurements with LCR Meter.

Bar winding resistance	18 mohm
Motor terminal resistance	46.4 mohm
Leakage inductance	0.24 mH
Total inductance	0.74 mH

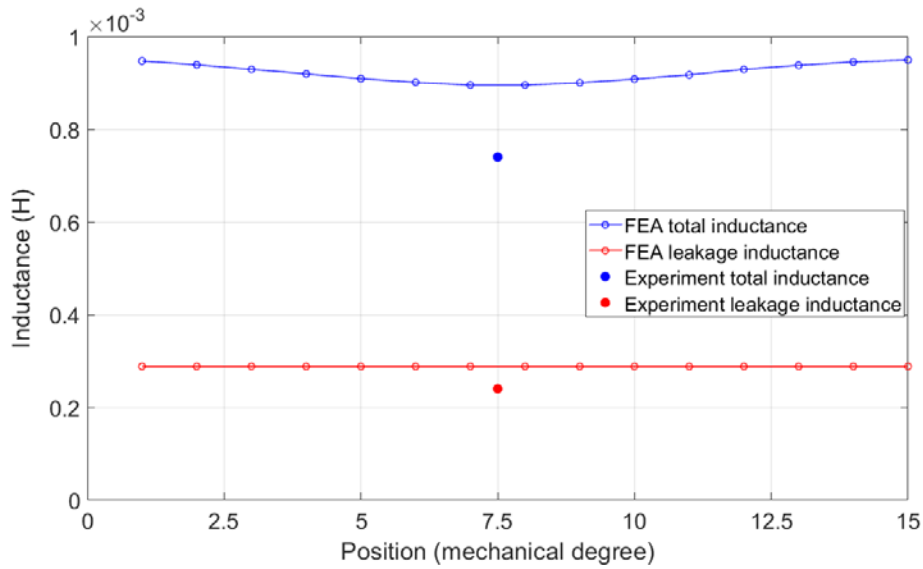


Figure 6.8. (a) Simulated and measured leakage and total inductances.

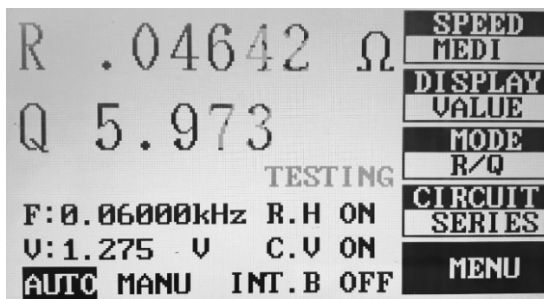


Figure 6.8. (b) Terminal resistance measurement using LCR meter.



Figure 6.8. (c) Total winding inductance measurement using LCR meter.

As mentioned in Chapter 4 of this dissertation, the unusual high inductance of the TFM offers unique features in field weakening operation. The characteristic current, as defined by the current

required to totally cancel the magnets' flux linkage, is actually smaller than the machine's rated current, making this TFM a so called "infinite drive system." In experimental setting, the characteristic current can be measured by operating the TFM as a generator with its two terminals shorted. This operation could not be done on regular PMSMs, for whom short-circuiting the terminals during operation would cause huge current and sudden braking torque. For this TFM, however, this operation is safe because its resulting short circuit current is much less than the rated current, thanks to the high stator reactance.

When operated as generator, the short circuiting current is calculated as:

$$I_{sc} = \frac{EMF}{\sqrt{R_s^2 + X_s^2}} \quad (1)$$

At higher speeds, the resistive impedance is much lower than the reactive impedance, such that the short circuit becomes:

$$I_{sc} \approx \frac{EMF}{X_s} = \frac{\omega \varphi_{PM}}{\omega L_s} = \frac{\varphi_{PM}}{L_s} \quad (2)$$

which is its characteristic current. The short circuit currents from FEA, experiment and theoretical equation, with the speed ranges from 5rpm to 400rpm, are plotted in Figure 6.9. For all the cases, the short-circuit currents settle to constant characteristic current values between 8A and 9A at above 300 rpm.

The result also revealed an interesting phenomenon that high inductance machines have the potential benefit in safety critical applications. In these high reliability applications, any terminal short circuit of a regular PMSM during operation would trigger a sudden spike in phase current,

which causes a high braking torque and possible demagnetization of the permanent magnets. The TFM, on the other hand, is safe from such a catastrophic scenario.

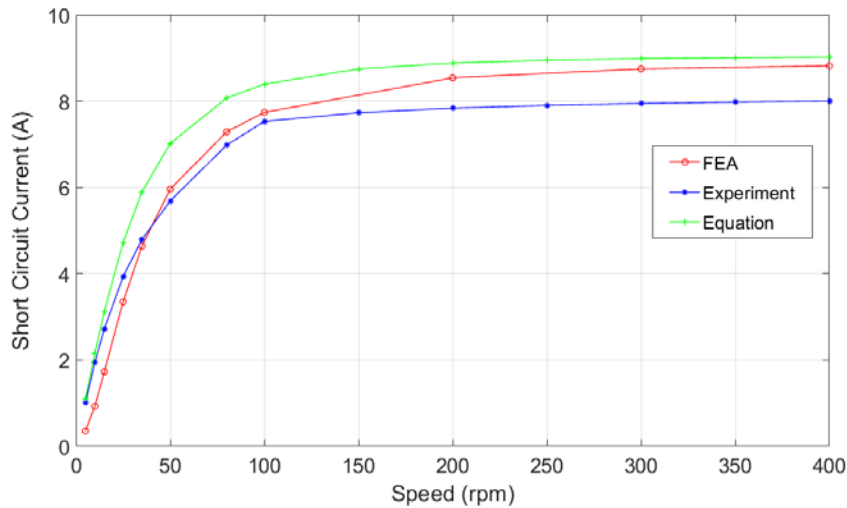


Figure 6.9. Simulated and experimental short circuit current at various speeds.

6.5 Heat Run

A heat run is conducted on the prototype motor to evaluate its thermal design. The motor is excited with rated current at 60A rms at the rated speed of 300 rpm. The test motor has Totally Enclosed Non Ventilated (TENV) cooling condition, with ambient temperature at 24 degrees Celsius. Temperature readings from the embedded thermal couples are recorded against time. The motor setup should eventually reach thermal steady state, and the recorded temperature at various parts inside the motor will then be used to verify the thermal simulation model. According to IEEE permanent magnet machine testing standard [2], thermal steady state is reached when the recorded temperature stay within 1 degrees Celsius for at least 30 minutes. However, for this experimental setup, the prototype TFM is mounted on a large testbed, which includes large pieces of metal baseplates that are in good thermal contact with the motor frame. As a result, those metal plates act as vast heatsinks that continuously draw heat from the motor frame. Consequently, true thermal

steady state is never reached even after a very long time of operation. In the end, the heat run is terminated after 160 minutes, when the temperature curves are very close to being flat. Even though the thermal steady state is not fully reached, the recorded temperatures, and especially the temperature gradients between the thermal couples, still provide valuable information on the thermal design of the prototype.

Figure 6.10 is the temperature plot from the heat run. In total, five thermal couples are attached to various parts of the prototype. As seen from the plot, one of the thermal couples failed for 45 minutes halfway through the heat run before miraculously recovered. With numbering from 101 to 105, these thermal couples are located at:

101.Surface of the insulation paper, inside of the stator core

102.Center of the winding

103.Surface of the stator core, inside of frame

104.Surface of the winding, inside of the insulation paper

105.Surface of the motor frame

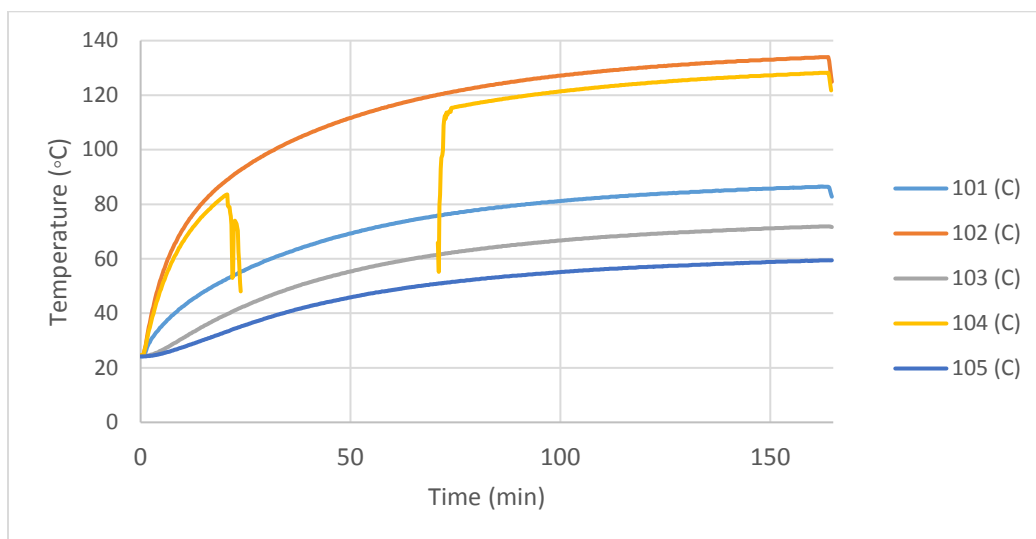


Figure 6.10. Heat run temperature measurements.

Because the vast majority of loss come from the stator copper loss, the temperature naturally is highest in the copper winding, and is lowest at the motor frame. From the plot, we observe that the temperature gradient is greatest between the winding temperature and the temperature outside the insulation paper. This is expected, and was predicted in the thermal simulation assuming the worst case scenario, in which the gap between the stator core and winding is not filled with insulation paper, but is filled with air. This low thermal conductivity air layer, conservatively assumed to be 0.25 mm thick, acts as thermal insulator that traps heat inside the coil. To improve upon this first generation prototype, tighter mechanical tolerance on the winding and stator dimensions could have reduced the gap in between. In addition, thermally conductive paste could have been used to fill the gap to increase its thermal conductivity.

Another observation is that between the center and surface of the winding, the 5 degree temperature gradient is rather small, which suggests the turns within the copper winding is in close contact with each other, and the turns at the center of the coil won't experience overheat. Additionally, the second largest temperature gradient is across the stator cores and magnets. At only 15 degrees, this gradient is expected because the thickness in this layer is quite high at 15mm. SMC and ferrite material, both have moderate thermal conductivity that are inferior to that of laminated steel. Finally, the 11 degree temperature gradient between the inside and outside of the motor frame is mostly caused by the adhesive and air mixture that bonds the stator to the frame. With more strict mechanical tolerance, the thickness of this layer can also be reduced. Overall, even though the experimentally measured temperatures confirm the final constructed prototype is at the worst case scenario for the thermal design, the highest winding temperature is only 134 degrees. This represents a 110 degree temperature rise, and is well below the 200 degree temperature rating of the magnet wire insulation material.

6.6 Result Discussion

Constrained by the limitation of the dyno setup, not every experimental test could be conducted to satisfaction. Nonetheless, all the possible test scenarios for a single phase motor have been performed with the best effort. The experimental results collected are thoroughly compared with those from the prototype-updated FEA model. From the experiment, the prototype's back-EMF constant, cogging torque, dc excitation torque, inductance and short circuit current all match the electromagnetic FEA simulation results to satisfying degrees. Thus, the FEA model and simulation method is validated to be trustworthy.

The validated FEA model could then be used in three ways. First, it is legitimate to assume that given better tolerance in the machine construction, and given ferrite magnets are true to the material property, the initial electromagnetic design and performance of the Stator-PM TFM in Chapter 4 can be realized. Secondly, all the three-phase machine performance aspects that cannot be tested with the single phase prototype, such as three-phase torque ripple, field weakening operation and efficiency map, could be simulated using the FEA three-phase TFM model. Thirdly, the next generation of TFMs could be designed and simulated using the same simulation method with increased confidence. Practical limitations in the motor construction and building process will also be thoroughly considered beforehand, such that the finished prototype motor would closely represent the optimal design.

Chapter 7 Contribution Summary and Future Work

The main research contributions of this dissertation can be summarized as below:

- This work thoroughly explored TFM topologies that make full use of rotor magnets and airgap area, and successfully address flux leakage issue.
- The author proposed a generalized inductance modeling method that links inductive components to key geometric parameters, and are used to reduce inductance.
- The proposed novel Stator-PM TFM topology is the best possible ferrite-magnet-based TFM design, with torque density comparable to a NdFeB-based TFM, and have various machine performance aspects addressed.
- Structural and thermal analysis helped successfully build single-phase TFM prototype, which demonstrates easy of construction.
- Experimental evaluation on the prototype motor validates FEA model, which is used to investigate three-phase TFM's unique performance aspects.

The suggested future work on this research topic include:

- Build a three-phase TFM prototype within the available motor housing, with improved mechanical tolerance that allows 1 mm air gap length.
- Conduct complete evaluation of three phase TFM with vector control.
- Explore potential of a high performance version of the same TFM topology, using laminated steel, liquid cooling and NdFeB magnets.

REFERENCES

- [1] M. R. Harris, G. H. Pajooman, and S. M. A. Sharkh, "Performance and design optimization of electric motors with heteropolar surface magnets and homopolar windings," in Proc. 1996 Inst. Elect. Eng., Elect. Power Appl., vol. 143, pp. 429–436.
- [2] B. C. Mecrow, A. G. Jack, and C. P. Maddison, "Permanent magnet machines for high torque, low speed applications", Proc. Int. Conf. on Electrical Machines (ICEM96), 1996,3,461-466.
- [3] Z. Rahman, "Evaluating radial, axial and transverse flux topologies for 'in-wheel' motor," Power Electronics in Transportation (IEEE Cat. No.04TH8756), 2004, pp. 75-81.
- [4] "ETM company information," [Online]. Available: <http://etmpower.com/>
- [5] Y. Huang, J. Zhu and Y. Guo, "Thermal Analysis of High-Speed SMC Motor Based on Thermal Network and 3-D FEA With Rotational Core Loss Included," in IEEE Transactions on Magnetics, vol. 45, no. 10, pp. 4680-4683, Oct. 2009.
- [6] D. Staton, A. Boglietti and A. Cavagnino, "Solving the More Difficult Aspects of Electric Motor Thermal Analysis in Small and Medium Size Industrial Induction Motors," in IEEE Transactions on Energy Conversion, vol. 20, no. 3, pp. 620-628, Sept. 2005.
- [7] S. M. Husband and C. G. Hodge, "The Rolls-Royce transverse flux motor development," Electric Machines and Drives Conference, 2003. IEMDC'03. IEEE International, 2003, pp. 1435-1440 vol.3.
- [8] Y. G. Guo, J. G. Zhu, P. A. Watterson and W. Wu, "Development of a PM transverse flux motor with soft magnetic composite core," in IEEE Transactions on Energy Conversion, vol. 21, no. 2, pp. 426-434, June 2006.

- [9] J. G. Washington et al., "Three-Phase Modulated Pole Machine Topologies Utilizing Mutual Flux Paths," in *IEEE Transactions on Energy Conversion*, vol. 27, no. 2, pp. 507-515, June 2012.
- [10] E. Muljadi, C. P. Butterfield, and Y. H. Wan, "Axial-flux modular permanent-magnet generator with a toroidal winding for wind-turbine applications," *IEEE Trans. Ind. Appl.*, vol. 35, no. 4, pp. 831–836, Jul./Aug. 1999.
- [11] US Patent US7830057 B2.
- [12] W. M. Arshad, T. Bäckström, and C. Sadarangani, "Analytical design and analysis procedure for a transverse flux machine," in *Proc. 2001 IEEE Conf. Elec. Mach. and Drives*, pp. 115–121.
- [13] O. Dobzhanskyi, R. Gouws and E. Amiri, "Comparison analysis of PM transverse flux outer rotor machines with and without magnetic shunts," *2016 IEEE Energy Conversion Congress and Exposition (ECCE)*, Milwaukee, WI, 2016, pp. 1-8.
- [14] M. R. Harris, G. H. Pajooman, and S. M. Abu Sharkh, "The problem of power factor in VRPM (transverse-flux) machines," in *Proc. 1997 IEEE Colloq. Electr. Machines Drives*, pp. 386–390.
- [15] P. Seibold, F. Schuller, M. Beez and N. Parspour, "Design and measurement of a laminated permanent magnet excited transverse flux machine for electrical vehicles," *2014 4th International Electric Drives Production Conference (EDPC)*, Nuremberg, 2014, pp. 1-6.
- [16] D. Svehkarenko, "On Design and Analysis of a Novel Transverse Flux Generator for Direct-driven Wind Application," PhD dissertation, Royal Institute of Technology, Stockholm, Sweden, 2010.

- [17] D. Oleksandr, "Study On Permanent Magnet Transverse Flux Machine," PhD dissertation, Dept. of Elec. and Computer Eng., Louisiana State Univ., 2012.
- [18] A. Ahmed, Z. Wan and I. Husain, "Permanent magnet transverse flux machine with overlapping stator poles," 2015 IEEE Energy Conversion Congress and Exposition (ECCE), Montreal, QC, 2015, pp. 791-798.
- [19] G. Yang, D. Cheng, H. Zhang, B. Kou, "Bidirectional crosslinking transverse flux permanent magnet synchronous motor", IEEE Trans. Magnetics, vol. 49, no. 3, pp. 1242-1248, 2013.
- [20] K. Lu, P. O. Rasmussen, and E. Ritchie, "Design considerations of permanent magnet transverse flux machines," IEEE Trans. Magn., vol. 47, no. 10, pp. 2804–2807, Oct. 2011.
- [21] K. Halbach, "Design of permanent magnet multipole magnets with oriented rare earth cobalt material," Nucl. Instrum. Methods, vol. 169, pp. 1–10, 1980.
- [22] Z. Wan, I. Husain, "Design, Analysis and Prototyping of a Flux Switching Transverse Flux Machine with Ferrite Magnets," 2017 IEEE Energy Conversion Congress and Exposition (ECCE), Cincinnati, OH, 2017.
- [23] K. Y. Lu, E. Ritchie, P. O. Rasmussem and P. Sandholdt, "Modeling and power factor analysis of a single phase surface mounted permanent magnet transverse flux machine," The Fifth International Conference on Power Electronics and Drive Systems, 2003. PEDS 2003., 2003, pp. 1609-1613 Vol.2.
- [24] A. M. El-Refaie, Z. Q. Zhu, T. M. Jahns and D. Howe, "Winding Inductances of Fractional Slot Surface-Mounted Permanent Magnet Brushless Machines," 2008 IEEE Industry Applications Society Annual Meeting, Edmonton, Alta., 2008, pp. 1-8.
- [25] D. C. Hanselman, Brushless Permanent-Magnet Motor Design, 1st ed.. McGraw-Hill: New York, 1994, pp.78–84.

- [26] "FLUX3D, User Guide," [Online]. Available: www.cedrat.com
- [27] S. J. Galioto, P. B. Reddy, A. M. EL-Refaie and J. P. Alexander, "Effect of Magnet Types on Performance of High-Speed Spoke Interior-Permanent-Magnet Machines Designed for Traction Applications," in *IEEE Transactions on Industry Applications*, vol. 51, no. 3, pp. 2148-2160, May-June 2015.
- [28] Z. Q. Zhu, Y. Pang, D. Howe, S. Iwasaki, R. Deodhar and A. Pride, "Analysis of electromagnetic performance of flux-switching permanent-magnet Machines by nonlinear adaptive lumped parameter magnetic circuit model," in *IEEE Transactions on Magnetics*, vol. 41, no. 11, pp. 4277-4287, Nov. 2005.
- [29] "Somaloy Prototyping Material, SPM," (Mar. 2016). [Online]. Available: <http://www.hoganas.com/somaloy>
- [30] T. Li and G. Slemon, "Reduction of cogging torque in permanent magnet motors," in *IEEE Transactions on Magnetics*, vol. 24, no. 6, pp. 2901-2903, Nov 1988.
- [31] K. M. Rahman, N. R. Patel, T. G. Ward, J. M. Nagashima, F. Caricchi and F. Crescimbeni, "Application of Direct-Drive Wheel Motor for Fuel Cell Electric and Hybrid Electric Vehicle Propulsion System," in *IEEE Transactions on Industry Applications*, vol. 42, no. 5, pp. 1185-1192, Sept.-Oct. 2006.
- [32] J. G. Washington, G. J. Atkinson and N. J. Baker, "Reduction of Cogging Torque and EMF Harmonics in Modulated Pole Machines," in *IEEE Transactions on Energy Conversion*, vol. 31, no. 2, pp. 759-768, June 2016.
- [33] S. Li, Y. Li and B. Sarlioglu, "Partial Irreversible Demagnetization Assessment of Flux-Switching Permanent Magnet Machine Using Ferrite Permanent Magnet Material," in *IEEE Transactions on Magnetics*, vol. 51, no. 7, pp. 1-9, July 2015.

- [34] T. Husain, I. Hasan, Y. Sozer, I. Husain and E. Muljadi, "Design considerations of a transverse flux machine for direct-drive wind turbine applications," 2016 IEEE Energy Conversion Congress and Exposition (ECCE), Milwaukee, WI, 2016, pp. 1-8.
- [35] "INTERFERENCE (PRESS & SHRINK) FIT CALCULATOR," [Online]. Available: <https://www.amesweb.info/InterferenceFit/InterferenceFit.aspx>
- [36] D. Staton, A. Boglietti and A. Cavagnino, "Solving the More Difficult Aspects of Electric Motor Thermal Analysis in Small and Medium Size Industrial Induction Motors," in IEEE Transactions on Energy Conversion, vol. 20, no. 3, pp. 620-628, Sept. 2005.
- [37] "Somaloy Prototyping Material," [Online]. Available: <https://www.hoganas.com/>
- [38] A. Ahmed, "Design and Optimization of a Novel Permanent Magnet Synchronous Machine Based on Transverse Flux Topology," PhD dissertation, North Carolina State University, Raleigh, North Carolina, 2018.
- [39] Group of authors, IEEE Trial-Use Guide for Testing Permanent Magnet Machines. 2014.